

METAL-STRONG INFLOWS AT THE OUTER-GALACTIC-SCALE OF A QUASAR

QIGUO TIAN^{1,2}, LEI HAO³, YIPENG ZHOU^{1,2,3,4,5}, XIHENG SHI^{1,2}, TUO JI^{1,2}, PENG JIANG^{1,2}, LIN LIN³, ZHENYA ZHENG³, HONGYAN ZHOU^{1,2,6}

Draft version January 3, 2025

ABSTRACT

We present an analysis of the absorption-line system in the Very Large Telescope/Ultraviolet and Visual Echelle Spectrograph spectrum at a redshift of $z_a = 3.1448$ associated with the quasar SDSS J122040.23+092326.96, whose systematic redshift is $z_e = 3.1380 \pm 0.0007$, measured from the H β +[O III] emission lines in our newly acquired NIR P200/TripleSpec data. This absorbing system, detected in numerous absorption lines including the N V, N III, C IV, C III, Si IV, Si III, and H I Lyman series, can be resolved into seven kinematic components with red-shifted velocities ranging from 200 to 900 km s⁻¹. The high-ionization N V doublet detected and the rather narrow Lyman series measured ($b \approx 14$ km s⁻¹) suggest that the absorption gas is photo ionized, possibly by the quasar. A low density is inferred by the fact that N III $\lambda 989.80$ is significantly detected while N III* $\lambda 991.51$ ($\log n_e = 3.3$ cm⁻³) is undetectably weak. A firm lower limit of a solar value to the abundance of the gas can be set based on the measurements of Si IV and H I column densities, as first proposed by F. Hamann. Detailed photoionization simulations indicate that T1, and possibly the absorber as a whole, has metallicities of $Z \sim 1.5 - 6.0 Z_\odot$, and is located at ~ 15 kpc from the quasar nucleus. The metal-strong absorption inflows at the outskirts of the quasar host galaxy is most likely originated in situ and were driven by stellar processes, such as stellar winds and/or supernova explosions. Such a relatively rare system may hold important clues to understanding the baryonic cycling of galaxies, and more cases could be picked out using relatively strong Si IV and weak Lyman absorption lines.

Subject headings: galaxies: active — quasars: absorption lines — quasars: individual (SDSS 122040.23+092326.96)

1. INTRODUCTION

Chemical evolution, i.e., the enrichment, dilution, and cycling of elements heavier than H and He, is one of the fundamental processes involved in galaxy evolution (e.g., E. Dwek 1998; M. Elvis 2006; B. C. J. Borguet et al. 2012a; A. Arcones & F. K. Thielemann 2023). Galaxies accrete the metal-poor gas from the intergalactic medium (IGM), which is then transformed into stars via star formation processes. The heavy elements are synthesized in the cores of stars, and with the death of these stars, these elements are further redistributed throughout the galaxies along with the baryonic cycling of galaxies. Outflows from galaxies can transport heavy metals over large distances, thereby enhancing the abundance of the circumgalactic medium or the IGM. Part of these gases

can later be re-accreted onto the galaxy, providing raw materials for the next generation of formation of stars and planets (e.g., C. Kobayashi et al. 2020). These processes constitute the framework that regulates the metal content of the galaxy and help shape the fundamental relationships involving the metallicities of galaxies. Therefore, studies on the metallicity of galaxies encode information about the star formation history of the galaxy and simultaneously provide insights into the complex processes that regulate the metal content, such as the large-scale gas inflows and outflows.

Quasars are extraordinarily luminous objects powered by the accretion of gas onto supermassive black holes (BHs; e.g., H. Netzer 2015). There is growing evidence that metal-rich outflows from quasars are important sources of metal enrichment to the interstellar medium (ISM)/IGM (e.g., F. Hamann et al. 2002; V. D’Odorico et al. 2004a, 2004b; S. Veilleux et al. 2005; S. K. Ballero et al. 2008; B. C. J. Borguet et al. 2012a; S. Lai et al. 2022). Indeed, observations by Chandra (F. Nicastro et al. 2005) have shown that the IGM has been enriched with heavy elements, far from having a primordial composition (T. Fang et al. 2002; M. Pettini 2004).

Quasars often exhibit abundant absorption and emission lines (R. J. Weymann et al. 1991), which are valuable tools for drawing information on chemical abundances (Z) (e.g., B. C. J. Borguet et al. 2012a). Compared with emission lines, absorption lines have certain advantages in abundance determinations, for example, they provide diagnostics that largely do not depend on the detailed understanding of the temperature and density (F. Hamann 1998). If the associated absorbing gas

¹ Polar Research Institute of China, 451 Jinqiao Road, Pudong, Shanghai 200136, People’s Republic of China; tianqiguo@pric.org.cn, zhouhongyan@pric.org.cn

² MNR Key Laboratory for Polar Science, Polar Research Institute of China, 451 Jinqiao Road, Pudong, Shanghai 200136, People’s Republic of China

³ Shanghai Astronomical Observatory, Chinese Academy of Sciences, 80 Nandan Road, Shanghai 200030, People’s Republic of China

⁴ School of Astronomy and Space Sciences, University of Chinese Academy of Sciences, 19A Yuquan Road, Beijing 100049, People’s Republic of China

⁵ School of Astronomy and Space Science, Nanjing University, Nanjing, Jiangsu 210093, People’s Republic of China

⁶ Key laboratory for Research in Galaxies and Cosmology of Chinese Academy of Science, Department of Astronomy, University of Science and Technology of China, Hefei, Anhui 230026, People’s Republic of China

happens to be located at large distance from the galaxy center (e.g., > 10 kpc), the metallicity inferred can be a unique probe to determine the properties of the host galaxy and its environment (F. Hamann & B. Sabra 2004; S. Veilleux et al. 2005; J. Tumlinson et al. 2017; H.-W. Chen et al. 2019).

According to their velocity ranges, the absorption-line systems in quasars can be empirically divided into three categories: broad absorption lines (BALs) with a typical velocity range exceeding 2000 km s^{-1} ; narrow absorption lines (NALs) with a velocity range less than 500 km s^{-1} ; and mini-BALs with intermediate velocity range in between the above two types (F. Hamann & B. Sabra 2004). It is normally believed that intrinsic NALs, mini-BALs, and BALs arise from different components of absorbing gas, or different regions of the same component (M. Elvis 2000; T. Misawa et al. 2007; H. Lu et al. 2008). Based on the type of observed absorption features, BALs, for example, are classified into high-ionization BALs (HiBALs) and low-ionization BALs (LoBALs; e.g., R. J. Weymann et al. 1991; P. B. Hall et al. 2002). Generally, HiBAL quasar spectra exhibit absorption lines of O VI $\lambda\lambda 1031.91, 1037.61$, C IV $\lambda\lambda 1548.19, 1550.77$, N V $\lambda\lambda 1238.82, 1242.80$, Si IV $\lambda\lambda 1393.76, 1402.77$ doublets, and H I Lyman series (e.g., B. C. J. Borguet et al. 2012a; P. Jiang et al. 2023). Meanwhile, LoBAL spectra show not only HiBALs, but also the absorption lines of Mg II $\lambda\lambda 2796.35, 2803.53$, Al III $\lambda\lambda 1854.72, 1862.79$, C II, Si II and N III, etc.

Exploring metal abundance using absorption lines is achieved by comparing observed and photoionization-simulated ion column densities of various elements in a 4D-parameter space involving the hydrogen column density (N_{H}), hydrogen number density (n_{H}), ionization parameter (U), and Z . For convenience, Z is defined to be the scaled value of the solar abundance. However, finding the best model in a 4D-parameter space (N_{H} , n_{H} , U , and Z) that can simultaneously reproduce the observed column densities of several ions is challenging.

F. Hamann (1997) suggested that lower limits on metallicities can be estimated using the combined information of H I Lyman series and certain high-ionization absorption lines. The values of the four parameters, including the Z are often determined iteratively by comparing the repeatedly refined model results with the observed line strengths (e.g., N. Arav et al. 2013; B. C. J. Borguet et al. 2013; W.-J. Liu et al. 2016; Q. Tian et al. 2019; X. Xu et al. 2019; Q. Tian et al. 2021). As shown in Appendix A, assuming that the spectral resolution and signal-to-noise ratio (S/N) are sufficiently high, the column density of H I can be measured over a wide range, from $\sim 10^{12} - 10^{13} \text{ cm}^{-2}$ to more than 10^{20} cm^{-2} , using Lyman absorption lines, Lyman-limit system, and damped Ly α wing.

Among the high-ionization absorption lines, the O VI $\lambda\lambda 1031.91, 1037.61$ and C IV $\lambda\lambda 1548.19, 1550.77$ absorption lines, normally seen in quasar spectra, are usually saturated, as oxygen and carbon are the two most abundant metallic elements in solar abundance (e.g., C. Allende Prieto et al. 2002). In addition, O VI absorption doublet lines could be contaminated by Ly α forest, and C IV absorption doublet lines are often mixed together due to the velocity separation being too small ($\sim 500 \text{ km}^{-1}$). In contrast, Si IV absorption doublet has some special advantages for measuring its column density: (1) Si IV does not suffer from the self-blending problem for NALs, and to some extent for mini-BALs, since the velocity separation for Si IV $\lambda\lambda 1393.76, 1402.77$ is $\sim 1933 \text{ km}^{-1}$, which is much larger than that of C IV doublet, (2) the abun-

dance of Si is lower than that of O and C by about 1 order of magnitude (e.g., N. Grevesse & A. J. Sauval 1998; H. Holweger 2001; C. Allende Prieto et al. 2002), thus, the saturation problem for the Si IV absorption lines is much weaker, (3) absorption lines associated with other ions of Si element, such as Si III $\lambda 1206.50$, Si II $\lambda\lambda 1260.42, 1526.71, 1808.01$ and Si II* $\lambda\lambda 1264.76, 1533.43, 1816.93$, if they could be detected, can also be used jointly with Si IV for diagnostics, as they a cover wide range in both the wavelength and oscillator strengths.

In the present work, we report the detection of the metal-strong inflows located at ~ 15 kpc from the center BH of the quasar SDSS 122040.23+092326.96 (hereafter SDSS J1220+0923), using absorption lines, such as the H I Lyman series, Si IV, N V, etc., obtained from the Ultraviolet and Visual Echelle Spectrograph (UVES) at the ESO's 8 m Very Large Telescope (VLT). An empirical formula for estimating the lower limit to metallicity is also given. This paper is organized as follows. The data we used will be described in Section 2. We analyze the absorption lines and calculate the corresponding ionic column densities in Section 3. We compare the observational results with photoionization calculations in Section 4 and discuss the results in Section 5. Our main findings are summarized in Section 6, along with the implications and future prospects.

2. OBSERVATIONS

SDSS J1220+0923 is a bright quasar discovered in Sloan Digital Sky Survey (SDSS; J. X. Prochaska et al. 2008). The first spectrum was obtained with the SDSS spectrograph on 2003 February 2 (K. N. Abazajian et al. 2009). The spectrum covers a wavelength range from 3800 to 9200 Å in the observed frame. The second spectrum was taken on 2012 January 21, using the Baryon Oscillation Spectroscopic Survey (BOSS) spectrograph (K. S. Dawson et al. 2013), providing an extended wavelength coverage of $\lambda \sim 3570 - 10350$ Å in the observed frame. These two spectra share a similar spectral resolution of $R \sim 2000$. The SDSS broadband photometry was carried out on 2003 April 27 (D. G. York et al. 2000). The magnitudes in the g , r , and i bands agree well with those of the synthetic photometry data obtained from the SDSS spectrum. The photometric monitoring of this object by the Catalina Survey⁷ (for 8 yr since 2005 April 6) obtained 419 observations, showing weak long-term variability of no more than 0.3 mag in the V band. We thus use the SDSS spectrum to recalibrate the BOSS spectrum, which is reported to suffer from a serious flux-calibration issue (K. S. Dawson et al. 2013). Assuming there are no prominent time variances of the quasar, we constructed a composite spectrum by combining the SDSS and BOSS spectra weighted according to their spectral S/Ns, which will be used for our further analysis.

A follow-up near-infrared (NIR) spectroscopic observation was carried out on 2023 April 9 at the Hale 200 inch telescope, using the TripleSpec spectrograph with a spectral resolution from 2500 to 2700. The NIR spectrum covers the rest-frame optical band (including the Mg II and H β regions). Four exposures were taken, each for 300 s. The seeing was about 1'' during the observations. The data was reduced with SpexTool (M. C. Cushing et al. 2004). The flux calibration and telluric correction were performed with an IDL program using the methods described in W. D. Vacca et al. (2003). The extracted flux agrees well with the United Kingdom Infrared Telescope

⁷ The Catalina surveys website site is <http://nesssi.cacr.caltech.edu/DataRelease/>

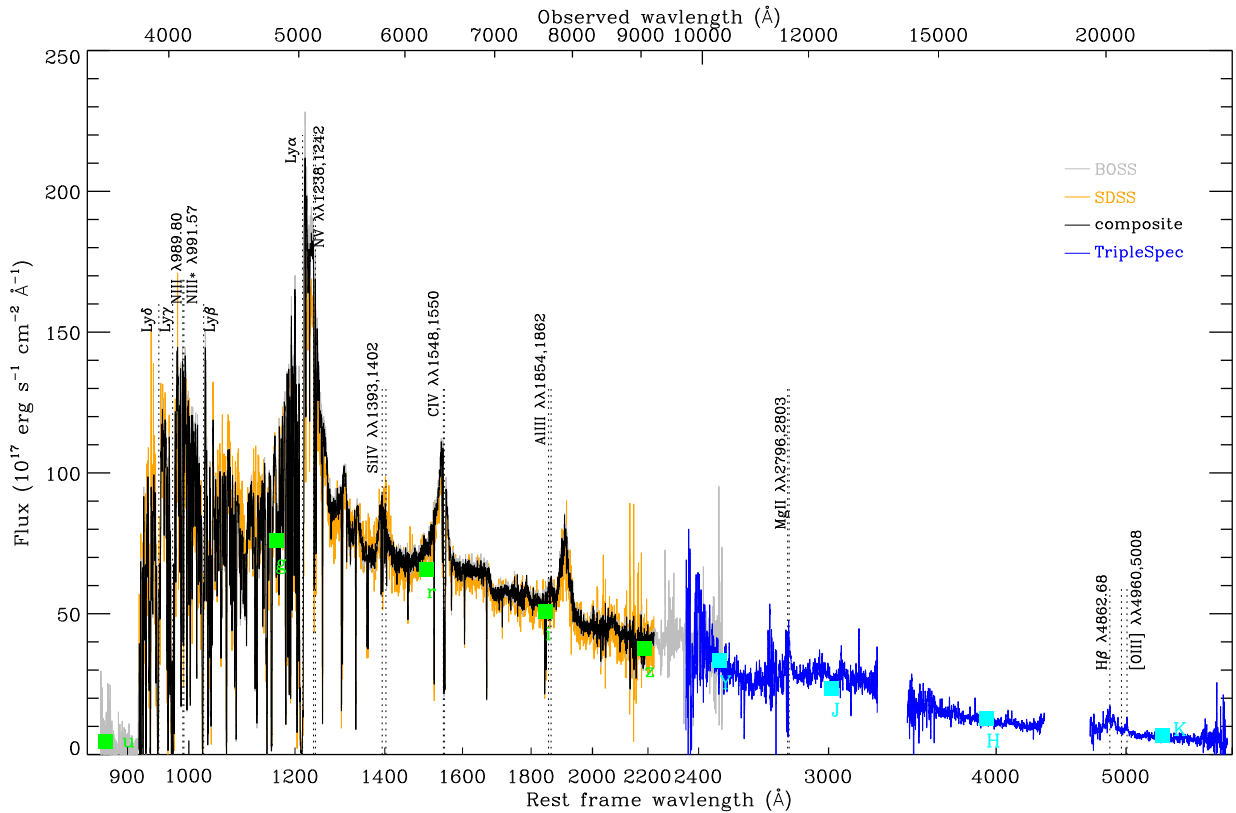


FIG. 1.— Rest-frame spectra of SDSS J1220+0923 from SDSS, BOSS, and TripleSpec. The green- and cyan-filled squares are photometric data from the SDSS and UKIDSS surveys. The TripleSpec spectrum (blue) presented has been smoothed for illustration purposes.

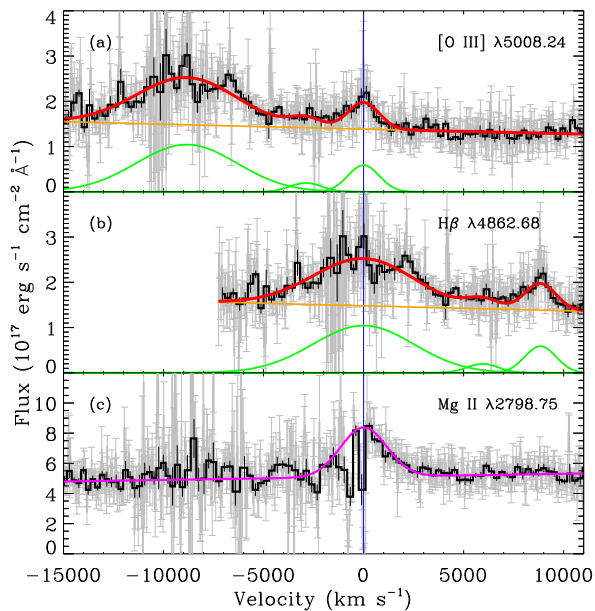


FIG. 2.— The TripleSpec spectrum of SDSS J1220+0923 showing (a) [O III] $\lambda 5008.24$, (b) H β $\lambda 4862.68$, and (c) Mg II $\lambda 2798.75$. The gray line is the observed spectrum, and the black line is the result rebinned using a weighted average of six data points for illustration purposes. The orange line in panels (a) and (b) represents the fitted power-law continuum in H β and [O III] region, the three green lines are the fitted Gaussian profiles for H β and [O III] emissions, and the red line is the total fitting result. The common velocity space is based on the redshift measured from H β and [O III]. The magenta line in panel (c) shows a Gaussian profile centered at 0 km s^{-1} , with the red wing matching the observed Mg II spectrum (the blue wing is contaminated), indicating that Mg II is consistent with the measured redshift.

(UKIRT) Infrared Deep Sky Survey (UKIDSS) $YJHK$ photometric data obtained in 2007 February 7.⁸ The NIR spectrum was used to calculate the systemic redshift, as it contains the [O III] $\lambda\lambda 4960.30, 5008.24$, and H β $\lambda 4862.68$ emission lines, with significances for H β and [O III] of about 13.3σ and 8.8σ , and a median spectral S/N in the H β and [O III] region of about 5.5. It has been suggested that emission lines such as the [O II] $\lambda 3728.48$, [O III] $\lambda\lambda 4960.30, 5008.24$ and H β $\lambda 4862.68$ can give good measurements of the systemic redshift (P. C. Hewett & V. Wild 2010; Y. Shen et al. 2016). We jointly fitted the NIR spectrum covering the H β and [O III] region, using the `mpfitexpr` procedure in IDL, to measure the systemic redshift. Each of the three lines was fitted by one Gaussian profile, and the flux ratio of [O III] $\lambda 5008.24 / \lambda 4960.30$ was fixed to the theoretical value of 2.98 (e.g., P. J. Storey & C. J. Zeppen 2000; M. S. Dimitrijević et al. 2007). The fitting result suggests a systemic redshift of 3.1380 ± 0.0007 , which is close to that observed by SDSS spectrum (~ 3.1400) (I. Pâris et al. 2018), and it will be used for further analysis in this work. After correcting for the Galactic reddening with $E(B-V) = 0.025 \text{ mag}$ (D. J. Schlegel et al. 1998; E. L. Fitzpatrick & D. Massa 2007), we transformed the photometric data, SDSS, BOSS, and composite spectra into the rest frame with the newly derived systemic redshift, as shown in Figure 1. Figure 2 shows the TripleSpec spectrum of H β , [O III], and Mg II emission lines along with the fitted results. The average rest-wavelength of Mg II emis-

⁸ The UKIDSS project is defined in A. Lawrence et al. (2007). UKIDSS uses the UKIRT Wide Field Camera (WFCAM; M. Casali et al. 2007). The photometric system is described in P. C. Hewett et al. (2006), and the calibration is described in S. T. Hodgkin et al. (2009). The pipeline processing and science archive are described by N. C. Hambly et al. (2008).

sion doublet (2798.75 Å) is taken from D. E. Vanden Berk et al. (2001), which is also applied by Y. Shen et al. (2016) to measure the quasar’s redshifts. The Mg II emission line, as shown in Figure 2(c), is consistent with the redshift determined from H β and [O III], further validating our redshift measurement.

In addition, UVES Spectral Quasar Absorption Database (SQUAD) released the high-resolution spectroscopic observations for SDSS J1220+0923 (M. T. Murphy et al. 2019) carried out using UVES (H. Dekker et al. 2000; S. Bagnulo et al. 2003) at European Southern Observatory’s (ESO’s) 8 m VLT on 2018 May 2.⁹ The exposure time for the observation was 12000 s and the spectroscopic resolution was $R \sim 40,000$. The released high-resolution normalized spectrum, covering a wavelength range of $\lambda \sim 3770\text{--}9467$ Å in the observed frame, will be the backbone data, allowing us to probe the properties of the absorbing gas in SDSS J1220+0923.

3. SPECTRAL ANALYSIS

3.1. Detected Absorption Lines

From the normalized high-spectral-resolution UVES spectrum, as shown in Figure 3, we identified the high-ionization absorption-line troughs of Si IV $\lambda\lambda 1393.76, 1402.77$, N V $\lambda\lambda 1238.82, 1242.80$, and C IV $\lambda 1548.19, 1550.77$; the low-ionization absorption troughs of N III $\lambda 989.80$, and C III $\lambda 977.02$; and the absorption troughs of H I Lyman series. The absorption system can be roughly divided into seven components ($T1$ to $T7$) within which the absorption is continuous. Each component contains one or several sub-kinematic components. The component $T1$, which has the smallest velocity, is the most clearly detached trough. The observed redshifts of the detected seven absorption components are from 3.1411 to 3.1497, as shown in Table 1, which are larger than the systemic redshift (~ 3.1380 , see Section 2), indicating that the absorption systems are redshifted. In this section, we will analyze the absorption lines and derive the column densities of the observed species. In the next section, these column densities will be used to derive the physical conditions of the inflowing gas.

3.2. Column Density Measurements

3.2.1. N V and Si IV

Figure 3(a)–(d) shows the N V $\lambda\lambda 1238.82, 1242.80$ and Si IV $\lambda\lambda 1393.76, 1402.77$ absorption lines. We label the seven sets of absorption trough components with different colors in Figure 3(a). To obtain the column densities of Si IV and N V (denoted as N_{SiIV} and N_{NV}), the rest-frame normalized spectrum covering the absorption regions of Si IV and N V was jointly fitted using Voigt functions, with the `mpfitexpr` and `walvogit` procedures in IDL. For each of the seven components, a different number of Voigt functions were used to characterize the optical depth ($\tau(\nu)$) for the troughs of the N V and Si IV doublets. The components $T1$ and $T6$ use one Voigt function, $T4$, $T5$, and $T7$ use two, while $T2$ and $T3$ use three and five Voigt functions, respectively. The redshift of each Voigt function associated with different transitions shares the same value. Meanwhile, the widths of the Si IV and N V absorption lines are considered as free parameters and are not required to be the same. Then, the constructed

optical depths for Si IV and N V were transformed into a modeled normalized spectrum by the following equation:

$$I_r(\nu) = (1 - C_f(\nu)) + C_f(\nu)e^{-\tau(\nu)}, \quad (1)$$

where C_f is the covering factor, which will be determined in the fitting. We fit the model to the normalized spectrum, and the results are shown in Figure 3, where the red ($T1$), green ($T2$), blue ($T3$), orange ($T4$), magenta ($T5$), purple ($T6$), and cyan ($T7$) lines indicate the seven absorption trough components. The C_f was fitted to be 0.986 ± 0.002 , indicating that the Si IV and N V absorbing gas fully obscure the central light source.

The ionic column densities can be obtained from the Voigt profile fitting, and the relationship between ionic column densities and optical-depth profiles is shown in Equation (2) (e.g., N. Arav et al. 2001),

$$N_{\text{ion}} = \frac{3.7679 \times 10^{14}}{f\lambda_0} \int \tau(\nu) d\nu (\text{cm}^{-2}). \quad (2)$$

The measured N_{SiIV} and N_{NV} are listed in Table 1. Meanwhile, the Doppler b parameter of the Si IV absorption line for component $T1$ is fitted to be $b_{\text{SiIV}} = 5.96 \pm 0.29 \text{ km s}^{-1}$, which will be used to estimate the gas temperature in Section 3.3 together with b_{HI} estimated in Section 3.2.3.

3.2.2. C III and C IV

The C III has an ionization potential of 47.89 eV, which is similar to that of Si IV at 45.14 eV. At the corresponding velocities, C III $\lambda 977.02$ exhibits absorption components similar to those observed in Si IV and N V, as shown in Figure 3(g). Additionally, the ionization potential of C IV is 64.49 eV, which lies between those of Si IV and N V (97.89 eV). Corresponding absorption components have also been observed at the respective velocities for C IV $\lambda 1548.19$ and C IV $\lambda 1550.77$, as shown in Figures 3(e) and (f).

We apply the same number of Voigt functions to fit the C III $\lambda 977.02$ absorption features as we did for Si IV and N V, except for components $T3$ and $T1$. Since $T3$ is heavily saturated, we employ only two Voigt functions (compared to five for Si IV and N V) to model its absorption. Meanwhile, $T1$ has a stronger absorption in C III compared to those of Si IV and N V doublets (each fitted with one Voigt function); thus, we use two Voigt functions to characterize its absorption feature. The fitted results for C III absorption lines are shown in Figure 3(g).

The velocity separation of the C IV absorption doublet is $\sim 500 \text{ km s}^{-1}$, which is smaller compared to those of N V ($\sim 960 \text{ km s}^{-1}$) and Si IV ($\sim 1930 \text{ km s}^{-1}$). Consequently, the blending of the C IV absorptions, observed between transitions of different systems, is due to the transitions of the doublet from the same system having such a small velocity separation. We use the same number of Voigt functions as for C III $\lambda 977.02$ to do the fitting for the C IV absorptions. It can be seen that the component $T1$ of C IV $\lambda 1548.19$ (Figure 3(e)) has a very broad absorption trough, indicating that it is likely contaminated. Therefore, we use the fitted profile of C III $\lambda 977.02$ of $T1$ as a reference to give an upper limit of N_{CIV} for this component. The fitted models are shown in Figures 3(e) and (f) for C IV $\lambda 1548.19$ and C IV $\lambda 1550.77$.

The C IV $\lambda 1548.19$ absorption trough of $T5$ is blended with the C IV $\lambda 1550.77$ absorption from $T1$, illustrated by the red dotted line in Figure 3(e) for the contribution from C IV

⁹ SQUAD is a database of 467 high-resolution quasar spectra from the data archive of VLT/UVES. The UVES spectroscopic data can be found at <https://data-portal.hpc.swin.edu.au/dataset/uves-squad-dr1>.

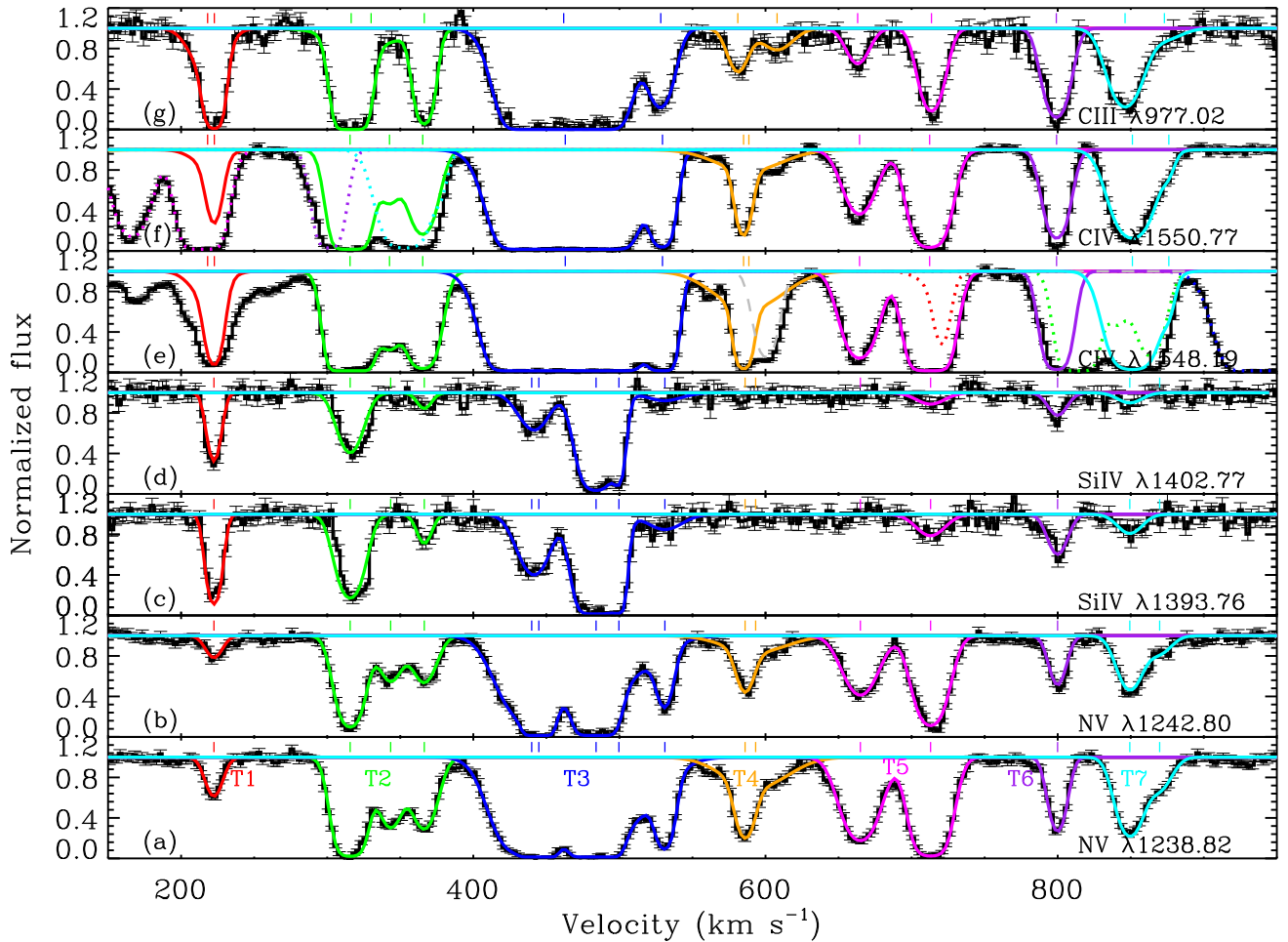


FIG. 3.— The absorption troughs of (a) N V $\lambda 1238.82$, (b) N V $\lambda 1242.80$, (c) Si IV $\lambda 1393.76$, (d) Si IV $\lambda 1402.77$, (e) C IV $\lambda 1548.19$, (f) C IV $\lambda 1550.77$, and (g) C III $\lambda 977.02$. The seven components, fitted using Voigt functions, are presented in different colors with solid lines. The blended features for C IV $\lambda 1548.19, 1550.77$ are presented with dotted lines in panels (e) and (f); see the text for the details. The dashed gray line in panel (e) indicates the contamination in the component T4 for C IV $\lambda 1548.19$. The solid red lines in panels (e) and (f) represent the modeled upper-limit absorptions of C IV $\lambda 1548.19, 1550.77$ for component T1, based on the corresponding C III $\lambda 977.02$ profile for this component; see the text for the details. The small vertical lines in each panel indicate the centers of the fitted components.

$\lambda 1550.77$ absorption. Similarly, the C IV $\lambda 1548.19$ absorption troughs of T6 and T7 are blended with the C IV $\lambda 1550.77$ absorption from T2, as shown by the green dotted line in Figure 3(e), marking the contribution from C IV $\lambda 1550.77$ absorption. In Figure 3(f), we show the contribution of C IV $\lambda 1548.19$ absorption from T5 to the C IV $\lambda 1550.77$ absorption trough of T1 with a magenta dotted line, and show the contribution of C IV $\lambda 1548.19$ absorptions from T6 and T7 in the C IV $\lambda 1550.77$ absorption trough of T2 with purple and cyan dotted lines. In addition, the component T4 for C IV $\lambda 1548.19$ is contaminated, as indicated by the dashed gray line in Figure 3(e). The measured column densities of C III and C IV are listed in Table 1.

3.2.3. Neutral Hydrogen

The normalized spectra of the H I Lyman series from Ly α up to Ly θ are presented in Figures 4(c)–(j). The velocity structures of Si IV $\lambda 1393.76$ and N V $\lambda 1238.82$, from Figure 3, are also shown in Figures 4(a) and (b), to compare with those of the H I Lyman series.

We estimated the N_{HI} for each absorption component by shifting the corresponding velocity centers of the modeled Si IV $\lambda 1393.76$ (and also N V $\lambda 1238.82$) profiles to those

of the Lyman series while adjusting the width and strength to match these absorption troughs. The relative optical-depth values τ_i of H I lines are set by the known oscillator strengths.¹⁰ The seven fitted absorption components are shown in red, green, blue, orange, magenta, purple, and cyan, respectively, in Figure 4. Although there are contaminations in the wavelength region of H I Lyman series, possibly from intervening H I absorption lines (C. R. Lynds 1967; R. J. Weymann et al. 1991), it is found that, for all seven components, there are at least two modeled Lyman absorption lines agree with the observations. Taking component T1 as an example, the modeled profiles can reproduce the troughs of Ly β and Ly ϵ simultaneously, and those of Ly δ , Ly η , and Ly θ are only slightly shallower than the observations. Since the $f_i \lambda_i$ of Ly β and Ly ϵ are quite different, with a ratio of about 11:1 between them, the simultaneous agreement between the models and observations gives us additional confidence in the measurement of N_{HI} . A chi-square corresponding to the best fit was denoted as χ_0^2 for each component. Then, the upper and lower limits of N_{HI} were calculated when the chi-squares were

¹⁰ $\tau_i = R \tau_{\text{Ly}\alpha}$, where $R = f_i \lambda_i / f_{\text{Ly}\alpha} / \lambda_{\text{Ly}\alpha}$ is the ratio of the optical depth of the Lyman series to that of Ly α , the f_i are the oscillator strengths, and the λ_i are the wavelengths of the lines.

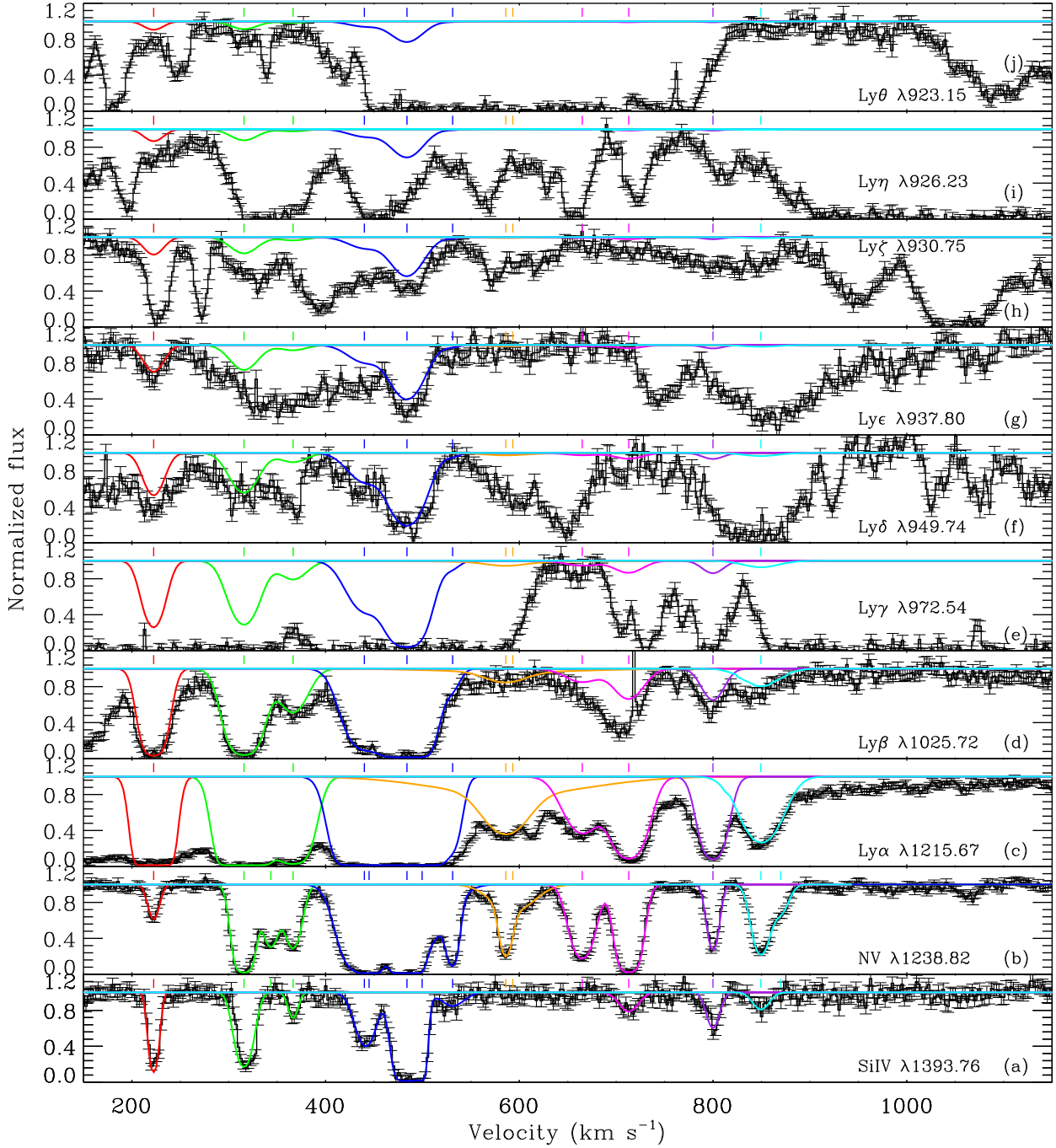


FIG. 4.— The normalized spectra in the Si IV, N V, Ly α , Ly β , Ly γ , Ly δ , Ly ϵ , Ly ζ , Ly η , and Ly θ regions with respect to Si IV λ 1393.76, N V λ 1238.82, Ly α λ 1215.67, Ly β λ 1025.73, Ly γ λ 972.54, Ly δ λ 949.74, Ly ϵ λ 937.80, Ly ζ λ 930.75, Ly η λ 926.23, and Ly θ λ 923.15. The red, green, blue, orange, magenta, purple, and cyan lines represent the seven absorption components. The small vertical lines in each panel indicate the centers of the fitted components.

$\chi_0^2 + 1$. The measured N_{HI} results are listed in Table 1. The Doppler b parameter of the H I Lyman absorption lines for component $T1$ is estimated to be $b_{\text{HI}} = 13.95 \pm 1.40 \text{ km s}^{-1}$, which will be used to estimate the gas temperature in Section 3.3 together with b_{SiIV} as shown in Section 3.2.1. The b_{HI} for the seven components are listed in Table 1.

3.2.4. Ground and Excited States of N III

We show the velocity structures of N III λ 989.80 and N III* λ 991.57, the ground and excited states for the N $^{2+}$ ion, in Fig-

ure 5. We also show the velocity structures of Si IV λ 1393.76 and N V λ 1238.82, replotted from Figure 3, in Figures 5(a) and (b), for comparison. The N III wavelength region shows clear absorptions at the velocities corresponding to those of Si IV and N V. The absorption component $T1$ is free from contamination; however, the other absorption components suffer from more or less contamination. We replotted the fitted Si IV λ 1393.76 total absorption profile to the N III and N III* regions, after applying a scale factor to match the absorption troughs associated with component $T1$ of N III and N III*, as

TABLE 1
ESTIMATED ABSORPTION-LINE PROPERTIES, IONIC COLUMN DENSITIES AND METALLICITIES OF THE ABSORBER IN SDSS J1220+0923

Parameters	<i>T</i> 1	<i>T</i> 2	<i>T</i> 3	<i>T</i> 4	<i>T</i> 5	<i>T</i> 6	<i>T</i> 7	Total
z_{abs}^a	3.1411	3.1424	3.1447	3.1461	3.1479	3.1491	3.1497	3.1447
$\log N_{\text{HI}} (\text{cm}^{-2})$	14.75 ± 0.05	14.83 ± 0.02	15.37 ± 0.02	13.80 ± 0.04	14.00 ± 0.01	13.73 ± 0.01	13.66 ± 0.01	15.59 ± 0.02
$b_{\text{HI}} (\text{km s}^{-1})$	13.95 ± 1.40	19.05 ± 1.90	22.99 ± 2.30	28.17 ± 3.00	23.64 ± 2.13	15.01 ± 1.50	25.35 ± 2.03	...
	...	19.00 ± 1.90	21.80 ± 2.30	105.64 ± 3.00	19.94 ± 1.79
	10.56 ± 2.30
$\log N_{\text{SiIV}} (\text{cm}^{-2})$	13.10 ± 0.03	13.32 ± 0.02	14.07 ± 0.02	< 12.240	12.48 ± 0.09	12.63 ± 0.05	12.36 ± 0.13	14.21 ± 0.02
$\log N_{\text{NV}} (\text{cm}^{-2})$	13.13 ± 0.04	14.43 ± 0.02	14.98 ± 0.02	13.85 ± 0.02	14.47 ± 0.01	13.55 ± 0.01	13.87 ± 0.01	15.24 ± 0.02
$\log N_{\text{CIII}} (\text{cm}^{-2})$	13.51 ± 0.04	14.05 ± 0.08	> 14.95	12.89 ± 0.05	13.29 ± 0.03	13.28 ± 0.03	13.30 ± 0.05	> 15.04
$\log N_{\text{CIV}} (\text{cm}^{-2})$	< 13.63	> 14.67	> 15.61	13.91 ± 0.04	14.47 ± 0.03	13.98 ± 0.03	14.21 ± 0.03	> 15.72
$\log N_{\text{NIII}} (\text{cm}^{-2})$	13.47 ± 0.06	< 13.70	< 12.88	< 13.02	< 12.76	...
$\log N_{\text{NIII}^*} (\text{cm}^{-2})$	< 12.82	< 13.04	< 13.79	12.64	< 12.20	< 12.35	< 12.08	< 13.95
$Z (Z_{\odot})$	1.50 ± 0.25	~ 3.25
$Z_{\text{min}} (Z_{\odot})$	1.50	2.08	3.08	2.12	2.25	5.76	3.77	2.49

Notes. The column densities are reported in logarithmic terms with units of cm^{-2} , while the metallicities are presented in their actual values relative to the solar abundance.

^a Redshifts of the absorption lines, calculated from N v absorption lines, are weighted by optical depths for individual components and the absorptions as a whole.

shown by the red and magenta lines in Figures 5(c) and (d). Assuming that N III absorbing gas has the same covering fraction as those of Si IV and N V, we use one Voigt function to fit the absorption trough of component *T*1, and the fitted result agrees well with the observation. The obtained N_{NIII} of component *T*1 is listed in Table 1. By shifting the modeled Si IV $\lambda 1393.76$ absorption profiles for components *T*2, *T*5, *T*6, and *T*7 to the N III wavelength and using them as templates to match the N III region, we estimated the upper limit of N_{NIII} for these components (except for the heavily contaminated components *T*3 and *T*4), and the results are listed in Table 1.

Different from the N III $\lambda 989.80$, N III* $\lambda 991.57$ does not have clear troughs at the velocity where the Si IV and N V show absorption troughs. By shifting the absorption profile of Si IV to the N III* velocity and using it as a template to match the N III* region, we estimated the upper limit of N_{NIII^*} , as listed in Table 1. A clear detection of N III $\lambda 989.80$ in combination with an almost nondetection of N III* $\lambda 991.51$ suggests that the absorbing gas is of low density (see Section 4.1).

3.3. Gas Temperature

The Doppler b parameter, contributed by both thermal and turbulent motions in gas, is described as (C. W. Finn et al. 2014)

$$b^2 = b_0^2 + \frac{2kT}{m}, \quad (3)$$

where b_0 represents the turbulent contribution to the line width, k is the Boltzmann constant, T is the gas temperature, and m is the atomic mass of the ions in question. Since H I and Si IV show a similar velocity structure (see Figure 4), we hypothesize that H I and Si IV absorptions arise from the same gas, implying that they have the same temperature and b_0 value. Consequently, the gas temperature can be derived as

$$T = \frac{b_{\text{HI}}^2 - b_{\text{SiIV}}^2}{2k\left(\frac{1}{m_{\text{HI}}} - \frac{1}{m_{\text{SiIV}}}\right)}. \quad (4)$$

Using the b values for H I and Si IV of the detached absorption component *T*1 estimated in Section 3.2.3 and 3.2.1, the gas temperature for this component can be estimated as $T = (9.99 \pm 2.76) \times 10^3 \text{ K}$.

4. PHYSICAL PROPERTIES OF THE ABSORBER

4.1. Hydrogen Number Density constraint

We employ the photoionization model generated with Cloudy version c17 (G. J. Ferland et al. 1998, 2017), in conjunction with the observed ionic column densities, to constrain the physical properties of SDSS J1220+0923. A slab-shaped dust-free model for absorbing gas with homogeneous density and scaled solar abundance is used to regenerate the measured ionic column densities. We applied the incident spectral energy distribution (SED), characterized primarily by a blackbody big bump (hereafter denoted as 4B SED), which is a superposition of a power-law UV bump component and a power-law X-ray component described as $\nu^{\alpha_{\text{UV}}} \exp(-h\nu/kT_{\text{BB}}) \exp(-kT_{\text{IR}}/h\nu)$ and $a\nu^{\alpha_{\text{X}}}$, respectively. They are extracted and combined from multiband observations (G. Zamorani et al. 1981; M. Elvis et al. 1994), and are considered typical for quasars (G. J. Ferland et al. 2017). The UV bump is parameterized by a UV power-law index $\alpha_{\text{UV}} = -0.5$ (M. Elvis et al. 1994), and is exponentially cut off with temperature $T_{\text{BB}} = 1.5 \times 10^5 \text{ K}$ at the high-energy end and $T_{\text{IR}} = 1580 \text{ K}$ at the low-energy end. The power-law X-ray component has an index $\alpha_{\text{X}} = -2$ greater than 100 keV and -1 between 13.6 keV and 100 keV (M. Elvis et al. 1994). The flux ratio of the X-ray to optical is $\alpha_{\text{OX}} = -1.4$ (G. Zamorani et al. 1981).

There are four parameters that are critical in characterizing the physical conditions of the absorbing gas: Z , U , n_{H} and N_{H} . The other properties, such as the distance (r_{abs}) of the gas to the central BH, the mass-flow rate (\dot{M}), and the kinetic luminosity (\dot{E}_{k}), can be derived from these four parameters (e.g., B. C. J. Borguet et al. 2012b). However, it is a challenge to find the best model that can simultaneously reproduce the observed column densities of multiple ions in a four-dimensional parameter space (U , n_{H} , N_{H} , and Z). Thus, we seek additional constraints on these four parameters to reduce the number of free parameters needed for the modeling.

The column density ratio between excited and ground states for the same ion depends on the electron density ($n_{\text{e}} \approx 1.2n_{\text{H}}$) and temperature (e.g., D. E. Osterbrock & G. J. Ferland 2006). The ion ratios, such as those for C II, Si II (e.g., B. C. J. Borguet et al. 2012b), N III, S III (e.g., C. Chamberlain & N. Arav 2015), and S IV (e.g., X. Xu et al. 2018, 2019), are often used to estimate the n_{H} by assuming a typical temperature, for instance, $T \simeq 10,000 \text{ K}$, for plasma photoionized by a quasar's spectrum (e.g., N. Arav et al. 2018). In this work,

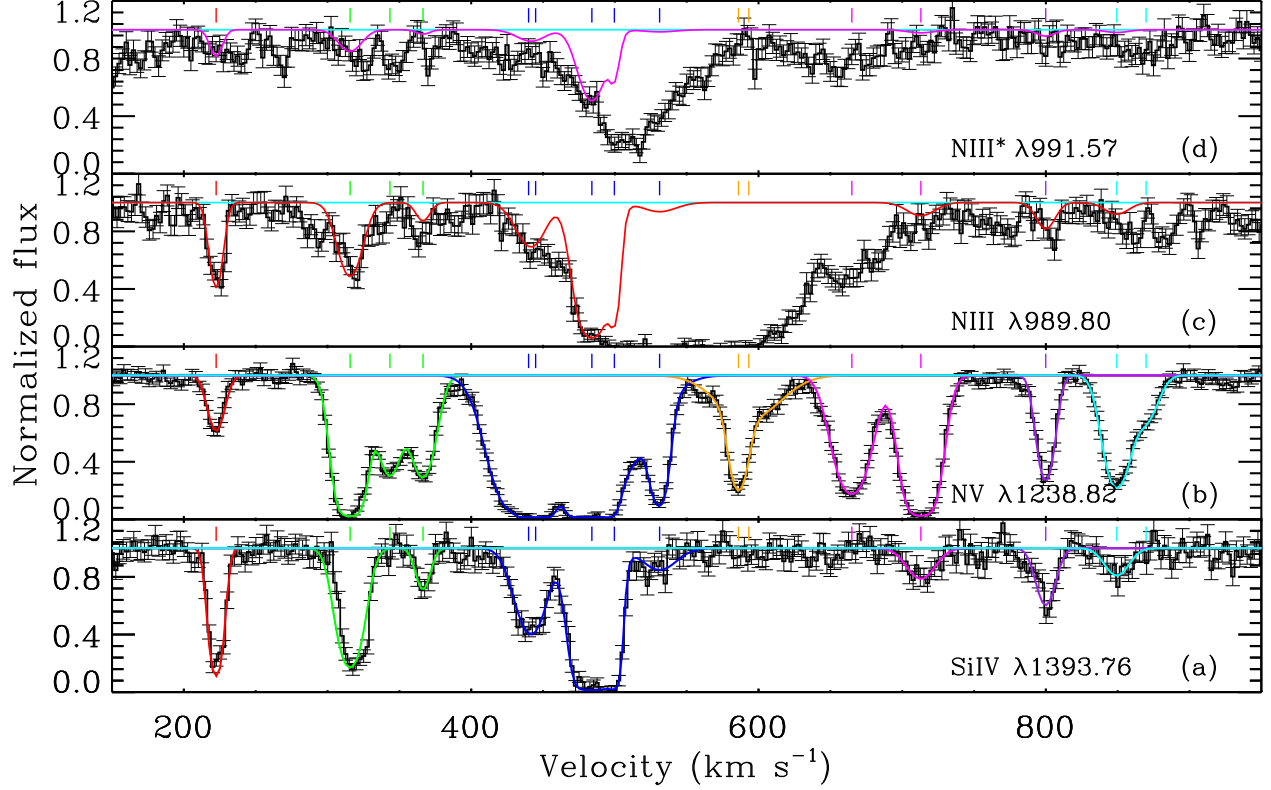


FIG. 5.— The normalized spectra in the N III and N III* regions with respect to N III $\lambda 989.80$ and N III* $\lambda 991.57$. The velocity structures of Si IV $\lambda 1393.76$ and N V $\lambda 1238.82$ are also replotted in panels (a) and (b) for comparison. The small vertical lines in each panel indicate the centers of the fitted components.

we use the ratio of $N_{\text{NIII}^*}/N_{\text{NIII}}$ to establish the relationship between n_{H} and (U, Z) under the condition when the simulated N_{HI} matches the observed value.

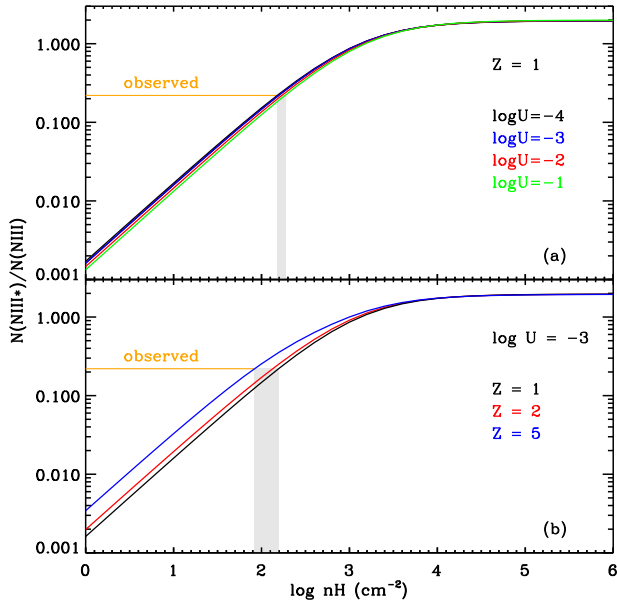


FIG. 6.— The simulated $N_{\text{NIII}^*}/N_{\text{NIII}}$ as a function of n_{H} , at the condition when the simulated N_{HI} reaches the observed value of component T1, for (a) $Z = Z_{\odot}$ with different U , and (b) $\log U = -3$ with different Z . The observed value of $N_{\text{NIII}^*}/N_{\text{NIII}}$ is indicated as the orange straight lines.

For a given $(U$ and $Z)$, the $N_{\text{NIII}^*}/N_{\text{NIII}}$ can be calculated

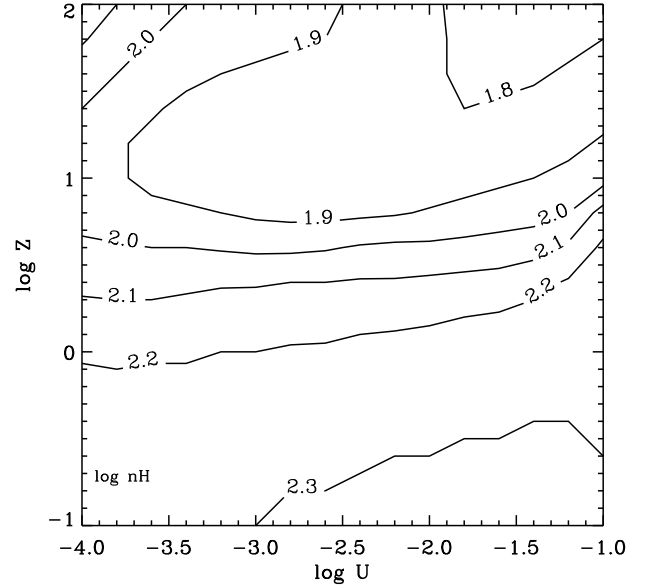


FIG. 7.— The n_{H} as functions of U and Z for component T1 obtained by the $N_{\text{NIII}^*}/N_{\text{NIII}}$ when the simulated N_{HI} reaches the observed value (see the text for the details). The corresponding N_{HI} contours are plotted in Figure 8.

as a function of n_{H} at the condition when the simulated N_{HI} at a given parameter set of $(U, Z, n_{\text{H}}(i))$ reaches the observed value (taking $\log N_{\text{HI}} = 14.754 \text{ cm}^{-2}$ for component T1 as an example). We plot the curves between $N_{\text{NIII}^*}/N_{\text{NIII}}$ and n_{H} for solar abundance with $\log U = -4, -3, -2,$ and -1 in Figure

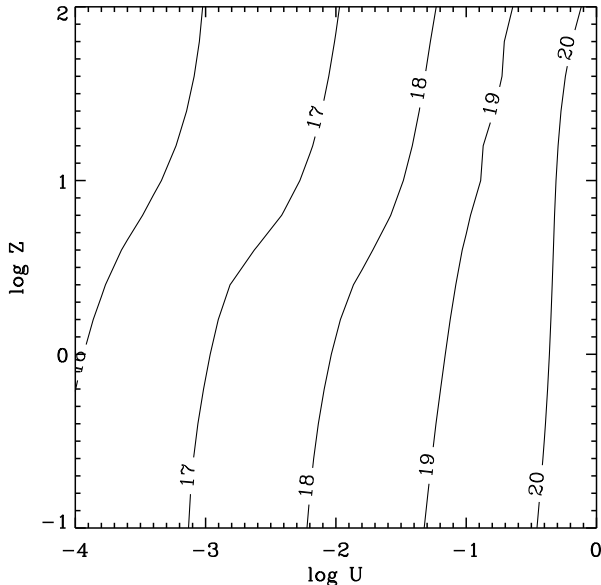


FIG. 8.— The N_{H} as a function of U and Z in the condition when the modeled N_{H1} reaches the observed value of component T1. The n_{H} values used to obtain the N_{H} contours are functions of U and Z , as shown in Figure 7.

6 (a), and for $\log U = -3$ with $Z = 1, 2,$ and 5 in Figure 6 (b). It can be seen that the curves are almost identical for different U at a fixed Z , while there are only slight differences when Z is different at a fixed U . This means that in the range of $1 \lesssim \log n_{\text{H}} (\text{cm}^{-3}) \lesssim 5$, the n_{H} can be determined from the ratio of N_{NIII^*} to N_{NIII} . Thus, the n_{H} for each given (U, Z) can be derived by the observed ratio between N_{NIII^*} and N_{NIII} . Then, the simulations were conducted over $-4 \leq \log U \leq -1$ and $-1 \leq \log Z \leq 2$, with a step of 0.2 dex. Consequently, the relations between n_{H} and $(U$ and $Z)$ can be built as

$$n_{\text{H}} = f(U, Z). \quad (5)$$

We plot the n_{H} and N_{H} contours, taking component T1 as an example, as a function of U and Z in Figures 7 and 8, respectively.

Therefore, with the help of the observed N_{H1} and the ratio of N_{NIII^*} to N_{NIII} , we are able to decrease the number of parameters for the model fitting from four ($U, n_{\text{H}}, N_{\text{H}}$, and Z) to two (U and Z). The best-fitting model that can simultaneously reproduce the observed column densities of detected ions can now be explored in a 2D parameter space (U and Z).

4.2. Results of the Best-fit Models

First, we estimated the U, Z, n_{H} and N_{H} for component T1. For a set value of $(U$ and $Z)$, n_{H} and N_{H} can be determined via the H I column density and the column density ratio between the excited and ground states of N III (Figures 7 and 8). With these four values, the absorption strengths of various metal ions were simulated, which can be compared with the observed absorption lines. In Figure 9, we show the parameter spaces in $(U$ and $Z)$ that are permitted and excluded by the observed column densities of different ions. The parameter spaces suggested by the measured column densities of Si IV and N V are shown as the blue and red regions, respectively. The best model is the intersection of these two areas, indicated by the green cross. It gives the best-estimated model of $\log U = -1.865 \pm 0.025$, $\log Z = 0.175 \pm 0.025$, $\log n_{\text{H}} = 2.203 \pm 0.008 \text{ cm}^{-3}$, and $\log N_{\text{H}} = 18.12 \pm 0.03 \text{ cm}^{-2}$. The

parameter space suggested by the measured temperature is shown as the gray region,¹¹ which covers the best model. The temperature, as an independent validation, provides us with additional confidence in the best model.

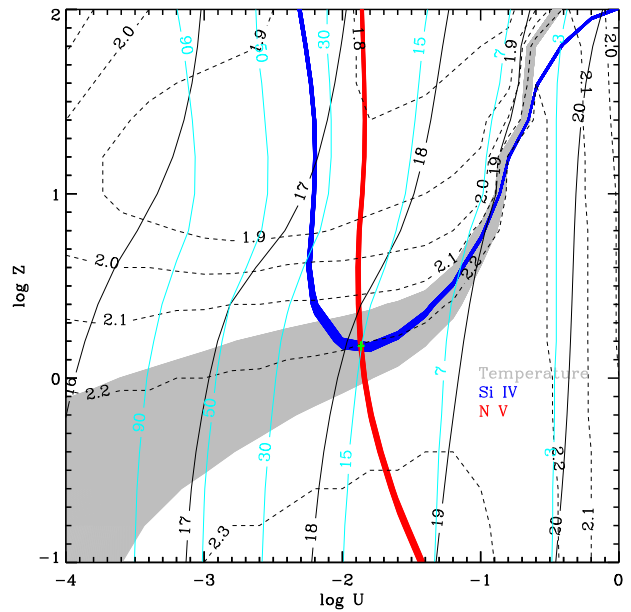


FIG. 9.— Photoionization models for component T1 in SDSS J1220+0923. The blue, red, and gray shaded regions represent the parameter space in $(U, Z, n_{\text{H}}$, and $N_{\text{H}})$ allowed by the observed N_{SiIV} and N_{NV} and temperature, within 1σ error. The black solid and dashed lines represent the n_{H} and N_{H} as functions of U and Z (see Figures 7 and 8). The cyan lines represent the location of the absorber (r_{abs}) as functions of U and Z . The best model is marked by the green cross. The errors of U, Z, n_{H} , and N_{H} are approximately estimated by the difference between the edge values of the intersection region and the best model.

In order to calculate the errors of the four parameters propagated from the error of N_{H1} , two figures similar to Figure 9 are drawn, using the upper and lower limits of N_{H1} as listed in Table 1, to derive the corresponding values of the four parameters, which are treated as the lower and upper limits. The errors of n_{H} and U , contributed from the error of N_{H1} , are negligible and thus ignored, while the errors of Z and N_{H} , resulting from the error of N_{H1} , are determined to be 0.05 and 0.060 dex, respectively. The values of Z and N_{H} , including the propagated errors, are updated as $\log Z = 0.175 \pm 0.075$, and $\log N_{\text{H}} = 18.12 \pm 0.09 \text{ cm}^{-2}$. The predicted column densities of N III, Si III, and Si II for component T1 by the best model in Figure 9 are $\log N_{\text{NIII}} = 13.77 \pm 0.03 \text{ cm}^{-2}$, $\log N_{\text{SiIII}} = 12.68 \pm 0.04 \text{ cm}^{-2}$, and $\log N_{\text{SiII}} = 11.18 \pm 0.08 \text{ cm}^{-2}$. This model also predicts $\log N_{\text{CIII}} = 14.34 \pm 0.03 \text{ cm}^{-2}$ and $\log N_{\text{CIV}} = 14.20 \pm 0.04 \text{ cm}^{-2}$ for component T1. The modeled N_{NIII} is larger than that of the measured result (see Table 1) by 0.3 dex, and the modeled N_{CIII} and N_{CIV} are larger than those of the measured results (see Table 1) by 0.8 and 0.6 dex, which will be discussed in Section 5.3.

With the measured n_{H} and U of the absorbing gas, the dis-

¹¹ For our source, the gas is relatively thin, resulting in minimal temperature variation inside. For example, the simulated temperature variation using the best model of ($\log U = -1.865$, $\log Z = 0.175$, $\log n_{\text{H}} = 2.203 \text{ cm}^{-3}$, and $\log N_{\text{H}} = 18.12 \text{ cm}^{-2}$) is only 241 K. Consequently, we selected the temperature at the outermost layer, corresponding to the N_{H} where the simulated N_{H1} reaches the measured value.

tance (r_{abs}) of the absorber away from the central source can be estimated. The definition of U is

$$U = \frac{Q_{\text{H}}}{4\pi r_{\text{abs}}^2 n_{\text{H}} c}, \quad (6)$$

where Q_{H} is the total rate of hydrogen-ionizing photons emitted by the central source (e.g., J. P. Dunn et al. 2010a). Q_{H} equals to $L(< 912)/\overline{E}_{\text{ph}}(< 912)$, where $L(< 912)$ is the ionizing luminosity of the continuum source, and $\overline{E}_{\text{ph}}(< 912)$ is the average energy for all ionizing photons. $Q_{\text{H}} = 1.73 \times 10^{57} \text{ s}^{-1}$, which is estimated by matching the flux of the model SED to the dereddened observed flux at 1450 Å in the SDSS rest-frame spectrum using a standard cosmology ($H_0 = 73.0 \text{ km s}^{-1} \text{ Mpc}^{-1}$, $\Omega_{\Lambda} = 0.73$, and $\Omega_m = 0.27$). The distance of component T1 was determined to be $14.8 \pm 0.5 \text{ kpc}$ for our best model.

We also experimented with the MF87 SED (W. G. Mathews & G. J. Ferland 1987) as an input to our models for component T1. The main difference between this SED and 4B SED is the location of their peaks, which are at approximately 3.0 and 0.5 Rydbergs, respectively. The best model results from the MF87 SED are $\log Z = 0.36 \pm 0.04$, $\log U = -1.95 \pm 0.015$, $\log N_{\text{H}} = 17.7 \pm 0.05$, $\log n_{\text{H}} = 2.1 \pm 0.02$, and $r_{\text{abs}} = 31 \pm 1 \text{ kpc}$. The U and n_{H} are only slightly smaller than those estimated from the 4B SED by 0.09 and 0.1 dex, and N_{H} is smaller than that from the 4B SED by 0.4 dex. The MF87 SED suggests a higher metallicity and further distance, with Z and r_{abs} values about twice the values in models using the 4B SED. In this work, we choose to use the model with the 4B SED to present our results. It can be seen that component T1 of the inflowing gas, located at $\sim 15 \text{ kpc}$ from the central BH, exhibits super-solar abundance even with the more conservative model using the 4B SED.

Second, we probe the nature of the absorber as a whole by assuming that it has an identical distance from the central BH as that of component T1. This assumption, upon inspection of Equation (6), suggests a relation of $n_{\text{H}} = 2.18/U$. As an attempt, assuming that the abundance of the absorber as a whole is the same as that of component T1, the total N_{SiIV} and total N_{NV} were calculated at the condition when the simulated N_{HI} matches the observed value. They are plotted as functions of U (also n_{H}) in Figure 10, as shown by the dashed blue and red lines. It can be seen that the simulated total N_{SiIV} over the range of $-4 \leq \log U \leq 0$ cannot reach the observed value, as shown by the horizontal green line. We then tried different metallicities near that of component T1 to search for the best U (and also n_{H}) that could simultaneously reproduce the observed total N_{SiIV} and total N_{NV} . It is found that the simulated N_{SiIV} and N_{NV} increased with increasing metallicity. The solid red and blue curves in Figure 10 show the simulated N_{SiIV} and N_{NV} for $Z = 3.54 Z_{\odot}$. The best model leads to $\log U = -1.31 \pm 0.02$, as indicated by the vertical orange and green lines, which can simultaneously reproduce the observed total N_{SiIV} and total N_{NV} . The corresponding hydrogen number density is $\log n_{\text{H}} = 1.66 \pm 0.03 \text{ cm}^{-3}$. The N_{H} is shown by the black line in Figure 10, and the best model is $\log N_{\text{H}} = 19.3 \pm 0.02 \text{ cm}^{-2}$. Furthermore, the N_{CIII} and N_{CIV} predicted by the best model are $\log N_{\text{CIII}} = 15.58 \text{ cm}^{-2}$ and $\log N_{\text{CIV}} = 15.78 \text{ cm}^{-2}$, which are consistent with the measured lower limits of N_{CIII} and N_{CIV} as shown in Table 1, serving as additional confirmation of the model. This characteristic Z value suggests that the inflowing gas in our source

could be metal-enhanced.

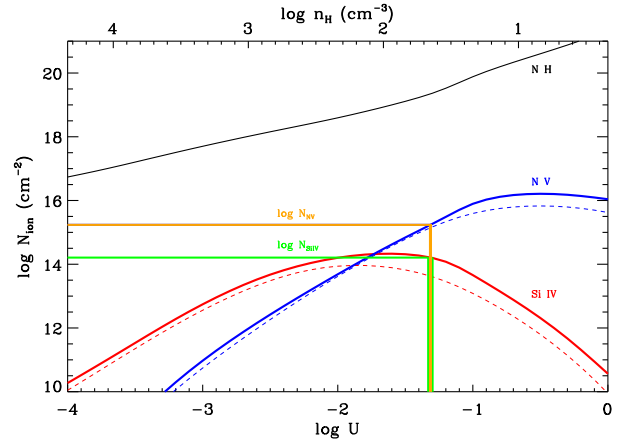


FIG. 10.— Photoionization models of the absorbing gas as a whole in SDSS J1220+0923 assuming the radial distance (r_{abs}) to central BH is identical to that of component T1 (see the text for the details).

It can be seen in Figure 3 that the relative strengths of the Si IV and N V absorption lines for component T1 are different from the other components. The N_{SiIV} and N_{NV} for component T1 are almost identical (see Table 1), while for all the other components, N_{SiIV} is lower than N_{NV} by about 1 dex. Since the ionization energy of N^{3+} is 77.47 eV (the energy required to create N^{4+} from N^{3+}), and is significantly larger than that of Si^{2+} at 33.49 eV, these differences suggest that the component T1 might have a smaller U than the other components. This further suggests that the component T1 has a larger n_{H} , see Equation (6), assuming the different components are located at the same distance from the central BH. Indeed, this is very likely true since the n_{H} of the absorber as a whole is $\sim 10^{1.66} \text{ cm}^{-3}$, less than that of component T1 at $\sim 10^{2.20} \text{ cm}^{-3}$.

5. DISCUSSION

5.1. The Nature and Origin of the Absorber

Through the detailed modeling, we have shown that the absorbing gas of SDSS J1220+0923 is at $\sim 15 \text{ kpc}$ from the central BH. This measurement is consistent with the absorbing gas having a low-density $n_{\text{H}} \sim 10^2 \text{ cm}^{-3}$ (see Section 4.2). The n_{H} is expected to be low for gas at larger distances from the central BH. Indeed, numerous studies have reported the properties of absorbers located at several or dozens of kiloparsecs, similar to SDSS J1220+0923 (e.g., $\sim 28 \text{ kpc}$, F. W. Hamann et al. 2001; $\sim 3.3 \text{ kpc}$, M. Moe et al. 2009; ~ 6 and $\sim 17 \text{ kpc}$, J. P. Dunn et al. 2010b; $\sim 3.7 \text{ kpc}$, K. Aoki et al. 2011; $> 3 \text{ kpc}$, D. Edmonds et al. 2011; $\sim 10 \text{ kpc}$, B. C. J. Borguet et al. 2012b; $\sim 3.4 \text{ kpc}$, N. Arav et al. 2013; $3.3\text{--}6 \text{ kpc}$, C. W. Finn et al. 2014). The n_{H} for these absorbers ranges from $10^{1.4}$ (D. Edmonds et al. 2011) to $10^{3.75} \text{ cm}^{-3}$ (M. Moe et al. 2009). They are considerably small compared with the absorbers located at parsec or dozens of parsecs distance from the central source (e.g., S. Zhang et al. 2015; W.-J. Liu et al. 2016; X.-H. Shi et al. 2016; S. Veilleux et al. 2016; Q. Tian et al. 2021). For example, the outflowing gas at $1\text{--}30 \text{ pc}$ from the central source is reported to have $7.5 < \log n_{\text{H}} < 9.5$ (M. de Kool et al. 2002).

Another intriguing feature of the absorbing gas of SDSS J1220+0923 is that it is red-shifted relative to the systematic

redshift of the quasar, suggesting it is an inflowing gas. Assuming that the absorbing gas can be described by a simple picture of a partially filled shell, the mass inflow rate can be estimated as (B. C. J. Borguet et al. 2012b),

$$\dot{M}_{\text{inflow}} = 4\pi r_{\text{abs}} \Omega \mu m_p N_{\text{H}} v, \quad (7)$$

where $\mu = 1.4$ is the mean relative atomic mass per proton, m_p is the mass of a proton, and Ω is the global covering factor of the inflowing gas clouds. The r_{abs} and N_{H} of the absorber as a whole have been obtained, as shown in Section 4.2. The $\tau(\nu)$ -weighted mean velocity, v , using Equation (1), calculated by the Si IV $\lambda 1402.77$ absorption lines is $\sim 470 \text{ km s}^{-1}$. Then, we have $\dot{M}_{\text{inflow}} \sim 20.0 \Omega M_{\odot} \text{ yr}^{-1}$. We roughly estimate the Ω using the detected fraction of NAL quasars with associated N V lines, which is $\sim 33\%$ reported by S. Perrotta et al. (2016). Then, the \dot{M}_{inflow} is estimated to be $\sim 6.6 M_{\odot} \text{ yr}^{-1}$.

Outflowing gases are generally metal-rich, suggested not only from simulations (e.g., C. R. Christensen et al. 2018; A. Vijayan et al. 2024), but also observations (e.g., M. L. Turner et al. 2015; J. Chisholm et al. 2018). In fact, solar or super-solar abundances in high-redshift Quasars have been reported across regions from their broad-line regions (BLRs) to those that are a few hundred kiloparsecs away (e.g., V. D’Odorico et al. 2004a, 2004b; S. Lai et al. 2022), suggesting that the metal enrichment by the outflow can be very efficient. There is direct evidence as well; for example, the outflows in UM 680, at a large distance of 70–120 kpc, have carbon and nitrogen abundances at least five times the solar value (V. D’Odorico et al. 2004a, 2004b). In contrast, the inflowing gas originating from primordial IGM is metal-poor (e.g., P. Dayal et al. 2013), and the metal abundance of inflows in Markarian 1486 is observed to be below 5% Z_{\odot} (A. J. Cameron et al. 2021). What is puzzling is where the metal-strong inflowing gas in our source, at ~ 15 kpc, comes from. There are some possible origins of the gas at 15 kpc scale, including (1) IGM, (2) a companion galaxy, (3) returning outflows, and (4) inflowing galactic winds. The first two origins are external, while the last two are internal.

Our absorber has a high metal abundance, making the first possible origin (the absorber coming from the IGM) quite unlikely. We checked the optical and NIR images of SDSS J1220+0923 from the SDSS and UKIDSS observations, and no companion galaxy was detected. However, the second potential origin cannot be ruled out, as the companion galaxy may be too faint to be detected, especially considering the relatively high systemic redshift. Additionally, the limited spatial resolution of the available images may not be able to resolve the companion galaxies.

The large distance, low-density, relatively low-velocity absorbing gas found in SDSS J1220+0923 is similar to that observed in IRAS F224546-5125 (B. C. J. Borguet et al. 2012b). However, the absorption lines in their source are blue-shifted, and they reported that their absorber exhibits characteristics of an outflowing galactic wind. Is it possible that the absorber in SDSS J1220+0923 is associated with an outflowing galactic wind, in that the outflow gas decelerates as it goes out and eventually falls back? The feasibility of this scenario can be considered together with the inflow velocity of the absorbing gas. For a returning outflow gas, the inflow velocity should be roughly consistent with the kinematics of the galaxy, as it is gravitationally bound to the galaxy. Typically, the rotation velocities of massive galaxies at ~ 15 kpc from their centers are $\lesssim 300 \text{ km s}^{-1}$ (A. Bosma 1978; S. M. Faber & J.

S. Gallagher 1979; M. Persic & P. Salucci 1995; E. F. Bell & R. S. de Jong 2001). While the observed velocity of component T1 at $\sim 220 \text{ km s}^{-1}$ can be consistent with the scenario, the high inflow velocities of other components, for example, $\sim 900 \text{ km s}^{-1}$ for component T7, are hard to accommodate in the picture. Even though our estimation of the distances has some uncertainties, and we cannot firmly exclude the ‘returning outflow’ scenario, we think this origin of absorbing gas is unlikely.

Meanwhile, if the absorbing gas that we see simply comes from one episode of a stellar wind and/or a supernova explosion, and if the gas is accidentally pushed in the direction that is away from us, we would naturally see it as an inflowing gas in our line of sight to the quasar. Interestingly, the high-abundance feature of our absorbing gas can be easily explained in the scenario, as the gas may contain heavy elements that are newly formed in the star. Stellar winds and/or supernova explosions typically have velocities at hundreds of kilometers per second (e.g., C. P. Johnstone et al. 2015), which is also consistent with the inflow velocities that we measured for the absorbing gas.

5.2. Diagnosis of High-metallicity Gas via the Absorption Lines

As shown in Figure 9, the column density of Si IV is sensitive to metallicities at the condition when the modeled N_{HI} reaches the observed value. We would like to further explore the diagnostic power of Si IV to the abundances by checking how N_{SiIV} varies with metallicity for different n_{H} and N_{HI} values. We carried out comprehensive photoionization simulations to do the investigation.

We assume a slab-shaped, homogeneous gas with 4B SED (see the details in Section 4.1). The simulations were run over $-4 \leq \log U \leq 0$ and $-2 \leq \log Z \leq 2$, for a given n_{H} , at the condition when the predicted N_{HI} reached a given value (e.g., observed value). The N_{SiIV} contour distributions for different N_{HI} (10^{12} , 10^{13} , 10^{14} , 10^{15} , and 10^{16} cm^{-2}) at each n_{H} varied from $\log n_{\text{H}} = 2.0$ to 10.0 cm^{-3} by 2.0 dex are plotted as black dashed lines in Figure 11. Also included in this figure are the N_{H} distribution contours (orange dashed lines). We indicated the measurable N_{SiIV} and N_{NV} ranges,¹² obtained by constructing Voigt profiles for the optical depths of the absorption lines whose line widths adopt the observed values for the absorption components in SDSS J1220+0923, as cyan regions. It can be seen clearly that the N_{SiIV} contour distributions are almost the same for different n_{H} that varied more than 10 orders of magnitude. N_{SiIV} is very sensitive to Z when the N_{HI} is relatively low at $\log N_{\text{HI}} < 16.5 \text{ cm}^{-2}$, indicating that the metallicity of the absorbing gas can be diagnosed by combining the information of N_{HI} and N_{SiIV} .

The minimum values of metallicity (Z_{min}), suggested by

¹² When the optical depth at the deepest point of the Si IV absorption trough is within the range of 0.05–3 (in this case, the corresponding residual flux ($e^{-\tau}$) is in the range of 0.95–0.05, and the line is neither too weak nor severely saturated (H. Zhou et al. 2019)), we think that the Si IV absorption lines can be detected and its column density can also be measured. Assuming a Voigt velocity profile with FWHM = 17.2 km s^{-1} , which is the average width of the Si IV absorption line for the components in SDSS J1220+0923, for the Si IV $\lambda 1402.77$ absorption line, the measurable N_{SiIV} is therefore $9.89 \times 10^{11} \text{ cm}^{-2} \leq N_{\text{SiIV}} \leq 5.78 \times 10^{13} \text{ cm}^{-2}$, indicating that the N_{SiIV} can be measured over ~ 2 orders of magnitude. Via similar analysis, the N_{NV} , with the FWHM to the measured average value (22.6 km s^{-1}) for the N V $\lambda 1238.82$, can be estimated to be in the range of $4.81 \times 10^{12} \text{ cm}^{-2} \leq N_{\text{NV}} \leq 2.81 \times 10^{14} \text{ cm}^{-2}$.

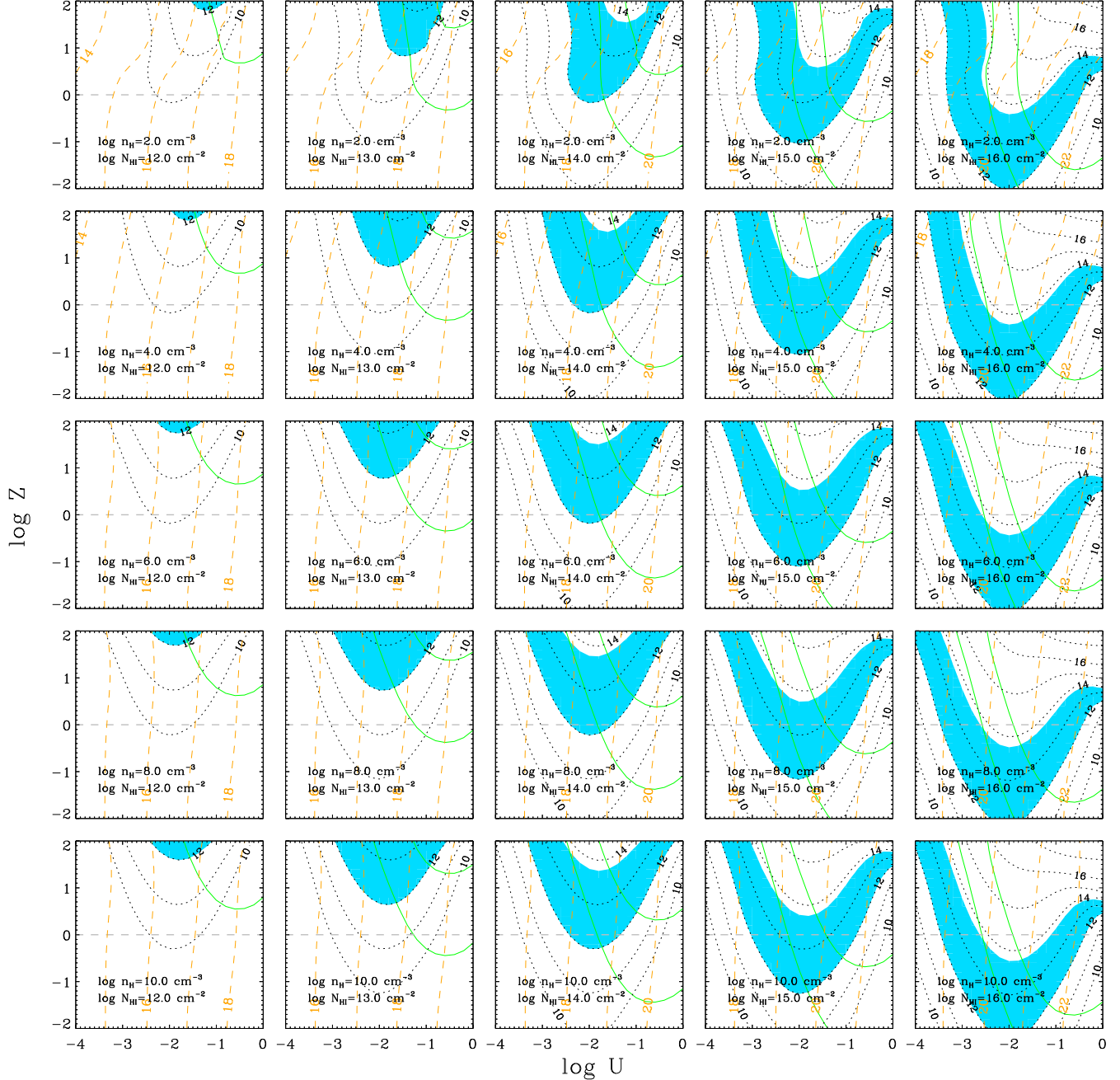


FIG. 11.— The simulated N_{SiIV} , for different N_{HI} (10^{12} , 10^{13} , 10^{14} , 10^{15} , 10^{16} cm^{-2}) at each n_{H} varied from $\log n_{\text{H}} = 2.0$ to 10 cm^{-3} by 2.0 dex, are plotted as functions of U and Z by black dotted contours. The cyan regions indicate the measurable regions of N_{SiIV} using Si IV $\lambda 1402.77$, assuming a Voigt velocity profile with a measured average FWHM of 17.2 km s^{-1} for our absorption components. These ranges are considered to be sensitive in measuring its column density as long as the optical depth at the line center is in the range of 0.05–3. Similarly, the two green contours show the measurable ranges for N_{NV} using N V $\lambda 1238.82$, with a measured average FWHM of 22.6 km s^{-1} . The N_{HI} for each panel is exhibited in orange contours.

N_{HI} and N_{SiIV} at $\log n_{\text{H}} = 4.0 \text{ cm}^{-3}$ (see Figure 11), were shown as functions of N_{HI} and N_{SiIV} in Figure 12. Also included in this figure are the Z_{min} values suggested by N_{HI} and N_{NV} at the same n_{H} . It can be seen that for the same value of N_{SiIV} and N_{NV} for a given N_{HI} , N_{SiIV} leads to a Z_{min} that is significantly higher than that derived from N_{NV} by approximately 1.8 dex. It is found that Z_{min} , suggested by N_{HI} and N_{SiIV} , can be well described by the following equation for

$$N_{\text{HI}} \lesssim 10^{16.5} \text{ cm}^{-2}:$$

$$\log Z_{\text{min}} = -0.994 \log N_{\text{HI}} + 0.940 \log N_{\text{SiIV}} + 2.537, \quad (8)$$

indicating that $\log Z_{\text{min}}$ increases linearly with the increase of $\log N_{\text{SiIV}}$ for a given N_{HI} , and decreases linearly with the increase of $\log N_{\text{HI}}$ for a given N_{SiIV} . It can be seen that the absorbing gas will have a relatively large Z_{min} when the N_{HI} is relatively small while the N_{SiIV} is relatively large. This phenomenon provides us with a way to search for absorbing gas with high metallicities.

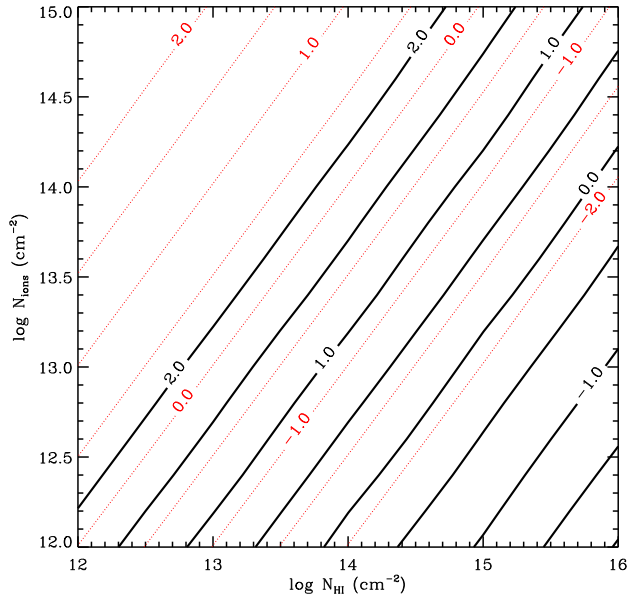


FIG. 12.— The minimum values of metallicity (Z_{\min}), suggested by N_{HI} and N_{SiIV} at $\log n_{\text{H}} = 4 \text{ cm}^{-3}$ (see Figure 11), are plotted as functions of N_{HI} and N_{SiIV} by the solid black line. Meanwhile, the Z_{\min} suggested by N_{HI} and N_{NV} is also exhibited, as shown by red dotted lines for comparison.

We use the measured total N_{HI} and total N_{SiIV} (see Table 1) to estimate the lower limit of the metallicity for the absorber as a whole in SDSS J1220+0923, and obtain its $Z_{\min} = 2.49 Z_{\odot}$, which is consistent with the estimated result of $\sim 3.54 Z_{\odot}$ in Section 4.2. The Z_{\min} for the seven components, determined using Equation (8), are $1.50 Z_{\odot}$ (T1), $2.08 Z_{\odot}$ (T2), $3.08 Z_{\odot}$ (T3), $2.12 Z_{\odot}$ (T4), $2.25 Z_{\odot}$ (T5), $5.76 Z_{\odot}$ (T6), and $3.77 Z_{\odot}$ (T7), all having supersolar metallicities. In particular, the component T6, with its N_{HI} exceeding N_{SiIV} by only 1.101 dex, exhibits metal abundances as high as $5.76 Z_{\odot}$. These estimated lower limits of metallicity are summarized in Table 1.

5.3. Nonsolar $[N/\text{Si}]$ and $[C/\text{Si}]$?

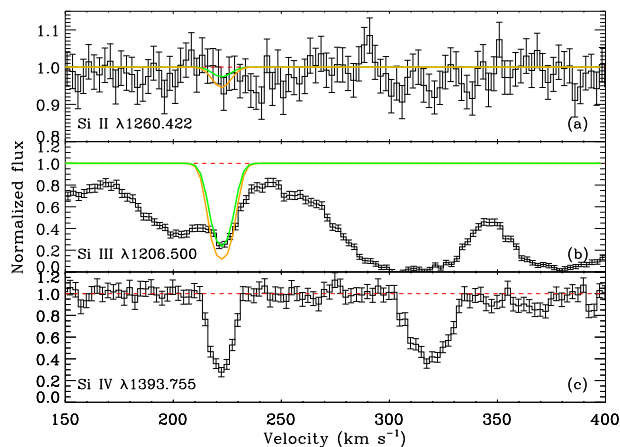


FIG. 13.— The normalized spectra for Si II $\lambda 1260.42$, Si III $\lambda 1206.50$, and Si IV $\lambda 1402.77$, respectively. The orange and green lines are the modeled absorption troughs of Si II $\lambda 1260.422$ (panel (a)) and Si III $\lambda 1206.500$ (panel (b)), with the column densities predicted by the best model using scaled solar abundance and reduced nitrogen abundance, assuming their optical-depth profiles are identical to that of Si IV.

The column densities of N III predicted by the best model of component T1, as shown in Section 4.2, is $\log N_{\text{NIII}} = 13.77 \pm 0.03 \text{ cm}^{-2}$. This is larger than that of the measured result (see Table 1) by 0.3 dex. This difference hints that the nitrogen abundance may deviate from that of the solar value. To illustrate this idea further, we plot a series of figures, similar to Figure 9, adopting scaled solar abundance except nitrogen. The results show that with the decrease in the abundance of nitrogen, the locus of the measured N_{SiIV} in the parameter space almost remains unchanged, and the locus of measured N_{NV} only moves slightly in the direction of larger U , while the predicted N_{NIII} gradually decreases. When the abundance of nitrogen is 0.4 times that of the scaled solar value, the predicted N_{NIII} matches that of the measured result. In this case, the best model results are $\log U = -1.705 \pm 0.025$, $\log Z = 0.200 \pm 0.025$, $\log N_{\text{H}} = 18.30 \pm 0.03 \text{ cm}^{-2}$, and $\log n_{\text{H}} = 2.205 \pm 0.005 \text{ cm}^{-3}$. The U , Z , and N_{H} are only slightly larger than those estimated from the best-fit scaled solar abundance modeling, as shown in Section 4.2, while the n_{H} is almost the same. The estimated distance is $12.3 \pm 0.5 \text{ kpc}$, which is similar to the result from the scaled solar abundance modeling ($14.8 \pm 0.5 \text{ kpc}$, Section 4.2).

Similarly, the best model for component T1 predicts N_{CIII} and N_{CIV} to be larger than the observed values, as detailed in Section 4.2. This discrepancy also suggests that the carbon abundance may deviate from the scaled solar abundance. Specifically, when the carbon abundance is reduced to 0.13 times that of the scaled solar value, the predicted N_{CIII} and N_{CIV} are in agreement with the observations.

The $\log N_{\text{SiIII}}$ of component T1 predicted by the best model using scaled solar abundance (Figure 9) and nonsolar N and C abundance are 12.68 ± 0.04 and $12.50 \pm 0.04 \text{ cm}^{-2}$, respectively. Meanwhile, the corresponding $\log N_{\text{SiII}}$ predicted are 11.18 ± 0.08 and $10.85 \pm 0.08 \text{ cm}^{-2}$. Assuming the optical depth of Si II and Si III have the same profiles as that of Si IV, we then reproduced the modeled absorption troughs of Si II $\lambda 1260.422$ and Si III $\lambda 1206.500$, using the column densities predicted by the best model with the scaled solar abundance and nonsolar N and C abundances, as the orange and green lines shown in Figure 13. It can be seen that the scaled solar abundance modeling is a little deeper than the observed trough, while the nonsolar N and C abundance modeling agrees with the observations. These experiments are all consistent with our speculation that the nitrogen and carbon abundance in the absorber might be lower than that of the solar values. Similar phenomena have also been reported in the literature (e.g., T. Zafar et al. 2014).

5.4. Ly α and Si IV sample

As we have demonstrated in Figures 11 and 12, the combined information of N_{HI} and N_{SiIV} can give indicative clues on the metallicities of the absorbers in quasars. We can use this idea to systematically search for quasars that may show high abundances. We search for the absorption-line quasars that show detectable Ly α , Si IV and N V absorption troughs. We focused on the intrinsic absorbers, and the selection criterion is based on the detectability of high-ionization N V absorption lines, as reported by S. Perrotta et al. (2016). To avoid contamination from the Ly α forests on N V absorption lines, we only selected absorption-line systems with velocities of $v > -5000 \text{ km s}^{-1}$. In addition, three quasars that had been checked before, having velocities outside of the above criteria, were also included in our sample. The details of the

sample selection for 28 absorption-line systems in 25 quasars are presented in Appendix B.

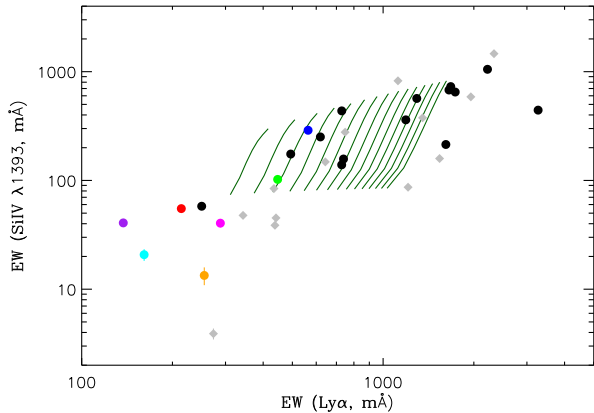


FIG. 14.— The measured EWs of Si IV $\lambda 1393.76$ presented as a function of those of Ly α for a quasar spectrum sample selected from VLT/UVES and Keck/HIRES spectra, based on the criteria that (1) velocities $> -5000 \text{ km s}^{-1}$, and (2) N V absorptions are detected. The gray-filled diamonds represent the inflows with red-shifted velocities $> 164 \text{ km s}^{-1}$, while the black solid circles represent absorption lines with blue-shifted velocities. The EWs for H I larger than 5000 mÅ are not presented for the sake of clarity. The red-, green-, blue-, orange-, magenta-, purple-, and cyan-filled circles are for components T1 to T7 of SDSS J1220+0923. The dark green lines indicate $Z_{\min} = Z_{\odot}$, plotted from Equation (8), where N_{HI} and N_{SiIV} are converted from the corresponding EWs with $b = 20\text{--}90 \text{ km s}^{-1}$ in a step by 5 km s^{-1} from left to right.

We plotted the measured equivalent widths (EWs) of Si IV $\lambda 1393.76$ versus those of Ly α , from Table 2 in Appdx B, in Figure 14. The red-, green-, blue-, orange-, magenta-, purple-, and cyan-filled circles represent the absorption components from T1 to T7 in SDSS J1220+0923. As shown in Figure 12, the absorber’s Z_{\min} can be estimated by N_{HI} and N_{SiIV} . Using the COG for a given b value, the ionic column densities can be derived from the EWs of the absorbing lines, as illustrated in Figure 15. We overplotted the $Z_{\min} = Z_{\odot}$ contour in Figure 12 to Figure 14 for b values ranging from 20 to 90 km s^{-1} in a step of 5 km s^{-1} , as shown by dark green lines. It can be seen that the absorbing components in SDSS J1220+0923 have small $\text{EW}_{\text{Ly}\alpha}$, reinforcing our result that they have supersolar metallicities.

There are 12 absorption-line systems in 12 quasars that exhibit red shifted absorption lines, with velocities $> 164 \text{ km s}^{-1}$, as presented in Table 2. The measured EWs of Ly α and Si IV, as shown in Figure 14 (gray-filled diamonds), imply the inflowing gas in these quasars might have high metal abundances. These objects will be further analyzed in the future.

6. SUMMARY, IMPLICATIONS, AND FUTURE WORKS

APPENDIX

A. SIMULATION OF N_{HI} RANGES USING LYMAN ABSORPTION LINES AND THE LYMAN-LIMIT SYSTEM

Figure 15 (a) shows the COGs of H I Lyman series, Ly α , Ly β , up to Ly θ , with $b = 250$ and 20 km s^{-1} . These two b values correspond to the absorption width of mini-BALs ($b = 250 \text{ km s}^{-1}$) and the typical Ly α forest ($b = 20 \text{ km s}^{-1}$) (E. M. Hu et al. 1995; L. Lu et al. 1996; T.-S. Kim et al. 1997), respectively. The COGs are divided into three parts: ‘linear’ part, ‘flat’ part, and ‘damping’ part (B. M. Peterson 1997). We plot the simulated Lyman absorption lines and the Lyman-limit system for

In summary, the high-redshift quasar SDSS J1220+0923 exhibits abundant absorption lines, which are close to the emission redshift of the quasar, with red-shifted velocity separation from the quasar systemic redshift ranging from 200 to 900 km s^{-1} . These include high-ionization species of N V, C IV, and Si IV, low-ionization species of N III, C III, and Si III, and absorption lines from H I Lyman series. The properties of the absorber were probed by jointly using absorption lines and photoionization simulations. The relationships between n_{H} and (U and Z), and between N_{H} and (U and Z) were established based on the measured column densities of N III, N III*, and H I. Thus, the four parameters (U , n_{H} , N_{H} and Z) of the absorbing gas are determined in a 2D parameter space. We found that the component T1 of the absorber has a metallicity of $\sim 1.54 Z_{\odot}$, and the absorber as a whole was determined to be $\sim 3.54 Z_{\odot}$. Meanwhile, the lower limits of metallicities of the other six components were also determined, and all exhibit supersolar values. It is intriguing to detect such a high-abundance inflow of gas in a quasar with a redshift of $z \sim 3$ when the Universe is still young. The metal-strong inflowing gas, located at $\sim 15 \text{ kpc}$, is most likely originated in situ and driven by stellar processes.

An empirical formula for estimating the abundance lower limit of absorbers, using the measured N_{HI} and N_{SiIV} , has been proposed. It suggests that metal-strong absorbers, such as remnants of supernovae, could be selected by relatively weak H I Lyman series and strong Si IV absorption lines.

A systematic study of the metallicities for quasar absorbers can be conducted in the future with methods as follows: (1) search for quasar spectra where absorption lines from H I Lyman series and N V doublet can be detected, indicating that they are likely intrinsic absorbers (S. Perrotta et al. 2016); (2) establish the relationship between n_{H} and (U and Z) using the H I absorption lines and low-ionization absorption lines from the ground and excited states, such as Si II, C II, and N III; (3) high-ionization absorption lines such as Si IV, C IV, and N V can be used to constrain metal abundance in the (U and Z) parameter space.

The authors thank the anonymous reviewer for the constructive suggestions. This work was jointly supported by the National Key R&D Program of China (grant Nos. 2022YFC2807300 and 2022YFF0503402), grant No. KJSP2020010102, the National Natural Science Foundation of China (NSFC; Nos. 11503023, and 12233005), and the Shanghai Natural Science Foundation (grant Nos. 19ZR1462500, 14ZR1444100, 20ZR1473600, 22ZR1481200, 21ZR1469800, and 21ZR1474200). This work has made use of data products from SDSS, UKIDSS, Catalina Sky Survey, data obtained through the UVES Paranal Observatory Project (ESO DDT Program ID 266.D-5655), and through the Telescope Access Program (TAP), which has been funded by the Strategic Priority Research Program The Emergence of Cosmological Structures (grant No. XDB09000000), National Astronomical Observatories, Chinese Academy of Sciences, and the Special Fund for Astronomy from the Ministry of Finance.

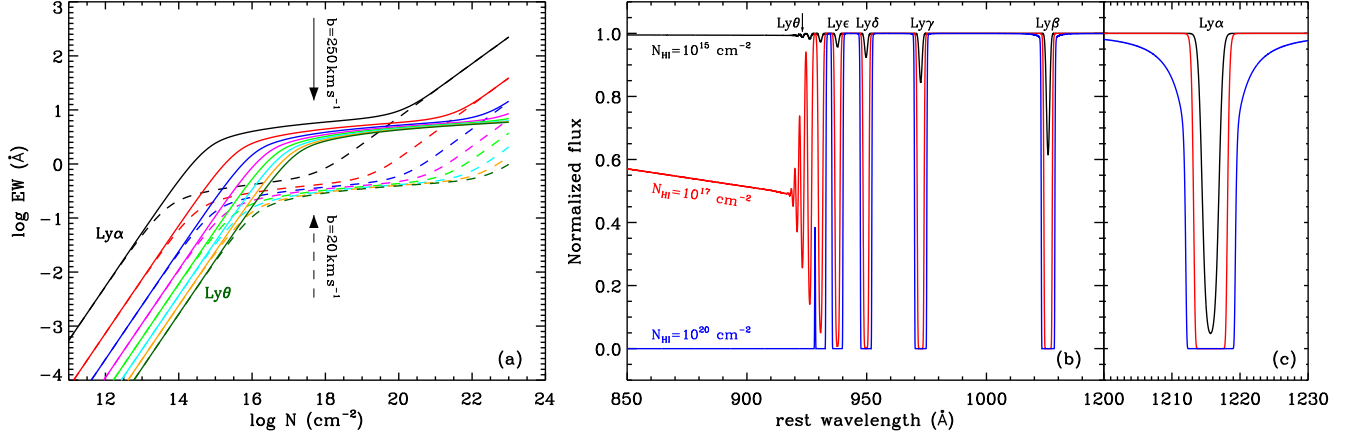


FIG. 15.— (a): COGs of absorption lines from Lyman series ($\text{Ly}\alpha$, $\text{Ly}\beta$ up to $\text{Ly}\theta$) with $b = 250 \text{ km s}^{-1}$ (solid lines) and $b = 20 \text{ km s}^{-1}$ (dashed lines). (b), (c): the simulated Lyman absorption lines and the Lyman-limit system, for $b = 250 \text{ km s}^{-1}$ at $N_{\text{HI}} = 10^{15}$, 10^{17} , and 10^{20} cm^{-2} , which are shown as black, red, and blue lines, respectively.

$b = 250 \text{ km s}^{-1}$ at typical N_{HI} values, corresponding to the three parts, in Figures 15 (b) and (c). To evaluate the N_{HI} ranges measured by Lyman absorption lines and the Lyman-limit system, we considered that they can be used to measure N_{HI} values when their residual flux is within the range of 0.95–0.05, in which they are neither too weak nor severely saturated (H. Zhou et al. 2019). For $b = 250 \text{ km s}^{-1}$, in the linear part, the lower limit of N_{HI} , estimated using the $\text{Ly}\alpha$ absorption line when the residual flux at the deepest point is 0.95 (0.05 for optical depth), is about $10^{13.4} \text{ cm}^{-2}$. Meanwhile, the upper limits of N_{HI} measured using $\text{Ly}\alpha$ and $\text{Ly}\theta$ when the residual flux at the deepest point is 0.05, are about $10^{15.8}$ and $10^{17.5} \text{ cm}^{-2}$. The Lyman absorption lines with wavelengths less than those of $\text{Ly}\theta$ are heavily blended (see Figure 15 (b)). Thus, for $b = 250 \text{ km s}^{-1}$ in the linear part, the measured N_{HI} range is about $10^{13.4}$ – $10^{17.5} \text{ cm}^{-2}$. At the same time, the estimated N_{HI} range that can be measured, in the linear part for $b = 20 \text{ km s}^{-1}$, is about $10^{12.3}$ (by $\text{Ly}\alpha$) to $10^{16.4} \text{ cm}^{-2}$ (by $\text{Ly}\theta$).

The optical depth of the Lyman-limit system for $\lambda \leq 912 \text{ \AA}$ is (H. Mo et al. 2010),

$$\tau(\lambda) = \left(\frac{N_{\text{HI}}}{1.62 \times 10^{17} \text{ cm}^{-2}} \right) \left(\frac{\lambda}{912 \text{ \AA}} \right)^3. \quad (\text{A1})$$

When the residual flux at 912 \AA is 0.95, the N_{HI} is $10^{15.9} \text{ cm}^{-2}$, which is considered the lower limit of N_{HI} that can be measured by the Lyman-limit system. The Lyman-limit system is powerful for measuring N_{HI} , as indicated by the measurable optical depth at specific wavelengths. For instance, when τ is 3 at λ of 714 \AA , with a residual flux of 0.95, the corresponding N_{HI} measured by the Lyman-limit system is 10^{18} cm^{-2} . For higher values of N_{HI} , it can also be measured by using a damped wing of $\text{Ly}\alpha$ absorptions (see Figure 15 (c) for $N_{\text{HI}} = 10^{20} \text{ cm}^{-2}$ as an example). Thus, it can be suggested that measuring N_{HI} is feasible in a remarkably wide range, from approximately 10^{13} to more than 10^{20} cm^{-2} , provided that the spectra are of a sufficiently high resolution and spectral S/N.

B. $\text{Ly}\alpha$ AND Si IV SAMPLE SELECTION

The sample is derived from two high-resolution quasar spectral data sets. The first is the continuum-normalized spectra in the public data release of the Keck Observatory Database of Ionized Absorption toward Quasars (KODIAQ) including DR1 170 quasars (J. M. O’Meara et al. 2015) and DR2 (130 quasars) (J. M. O’Meara et al. 2017), at a redshift range of $0.07 < z_c < 5.29$, observed with the High-Resolution Echelle Spectrograph (HIRES; S. S. Vogt et al. 1994) at the Keck I telescope. The second consists of 476 quasars with continuum-normalized spectra from the first data release of SQUAD (M. T. Murphy et al. 2019), with a redshift range of $z_c = 0.01$ – 6.31 , observed with VLT/UVES (H. Dekker et al. 2000).

Our search focused on the so-called associated absorption lines (C. B. Foltz et al. 1986; F. Hamann & B. Sabra 2004), using the detectability of the N V absorption doublet as a criterion, which offers the best statistical tool to identify intrinsic systems, as reported by S. Perrotta et al. (2016). We also rejected the objects where the Si IV doublet absorption troughs are heavily blended.

We calculated the rest-frame EWs for the absorption trough of $\text{Ly}\alpha$, Si IV doublet, and N V doublet for each absorption system in the sample, and listed the results for 28 absorption systems in 25 quasars in Table 2. We have determined the systemic redshifts for each source in the sample, employing emission lines in decreasing order of accuracy: O I, [O III], Mg II, and C III] (Y. Shen et al. 2016), if they could be observed. The measured redshifts are detailed in Table 2, with the specific emission line used indicated. For sources in the first SQUAD data release, we use the VLT/UVES spectra (H. Dekker et al. 2000) to measure redshifts. On the other hand, for the sources in the KODIAQ data release, we use the SDSS spectra, as only normalized spectra have been released (J. M. O’Meara et al. 2015, 2017). It is worth noting that, for one of the sources (J012227.89-042127.1), we also conducted NIR spectroscopic observations on 2020 October 6, using the Hale 200 inch telescope with the TripleSpec spectrograph, and the systemic redshift was measured using the [O III] $\lambda 5008.24$ emission line. With the measured redshifts, the weight-averaged

TABLE 2
LY α AND Si IV SAMPLE

Source	z_{em}	v_{ave}^a (km s $^{-1}$)	EW (Ly α) (mÅ)	EW (Si IV) (λ 1393, mÅ)	EW (Si IV) (λ 1402, mÅ)	EW (N V) (λ 1238, mÅ)	EW (N V) (λ 1242, mÅ)	Sample
J001602.40-001225.1	2.0918 \pm 0.0002 ^b	-6161.40	1189.3 \pm 1.4	360.6 \pm 3.9	219.3 \pm 4.3	< 219.6 \pm 0.6	75.6 \pm 0.8	SQUAD
J004131.43-493611.5	3.2331 \pm 0.0009 ^c	-85.10	1615.1 \pm 1.8	214.0 \pm 1.4	185.5 \pm 1.2	116.2 \pm 2.0	64.2 \pm 2.2	SQUAD
J010604.41-254651.3	3.3794 \pm 0.0002 ^b	-1271.40	3268.1 \pm 2.1	442.9 \pm 6.9	315.6 \pm 6.1	621.1 \pm 4.8	428.1 \pm 5.1	SQUAD
J010821.72+062327.1	1.9692 \pm 0.0001 ^b	-3484.46	1734.8 \pm 2.2	649.7 \pm 3.3	549.8 \pm 3.2	167.8 \pm 3.4	101.8 \pm 3.4	SQUAD
J012227.89-042127.1	1.9703 \pm 0.0002 ^d	-613.53	1676.7 \pm 21.2	729.1 \pm 7.4	635.2 \pm 8.8	1454.0 \pm 17.6	1564.6 \pm 20.4	SQUAD
J012227.89-042127.1	1.9703 \pm 0.0002 ^d	164.53	1539.5 \pm 18.3	159.0 \pm 9.4	131.5 \pm 8.8	< 911.3 \pm 15.0	438.2 \pm 20.2	SQUAD
J013857.44-225447.3	1.8961 \pm 0.0001 ^c	255.49	1954.8 \pm 1.5	587.1 \pm 5.0	474.5 \pm 5.1	679.5 \pm 4.9	504.3 \pm 5.6	SQUAD
J022620.49-285750.7	2.1750 \pm 0.0001 ^c	-189.29	250.1 \pm 0.8	57.9 \pm 1.8	42.5 \pm 1.8	165.7 \pm 1.5	127.4 \pm 1.5	SQUAD
J030640.90-301031.6	2.0997 \pm 0.0005 ^c	-8346.26	1293.3 \pm 16.5	567.3 \pm 19.2	432.6 \pm 21.4	415.2 \pm 8.3	336.2 \pm 8.5	SQUAD
J030643.75-301107.7	2.1191 \pm 0.0001 ^c	-597.44	2220.0 \pm 5.6	1051.5 \pm 48.3	683.8 \pm 41.8	1630.1 \pm 12.4	1591.4 \pm 14.1	SQUAD
J030643.75-301107.7	2.1191 \pm 0.0001 ^c	-70.64	738.9 \pm 3.8	157.4 \pm 23.0	272.6 \pm 21.2	214.6 \pm 6.9	202.5 \pm 17.0	SQUAD
J031006.09-192124.0	2.1434 \pm 0.0001 ^e	-1947.55	728.8 \pm 2.2	139.1 \pm 3.3	145.9 \pm 2.9	163.5 \pm 1.6	141.2 \pm 2.3	SQUAD
J031009.09-192207.2	2.1239 \pm 0.0001 ^e	-176.97	619.3 \pm 1.7	251.2 \pm 4.3	220.8 \pm 4.2	74.2 \pm 2.0	35.1 \pm 3.4	SQUAD
J040356.64-170321.8	4.2423 \pm 0.0001 ^b	-670.19	729.1 \pm 1.1	< 435.9 \pm 4.0	< 361.7 \pm 4.7	51.6 \pm 1.8	32.9 \pm 1.8	SQUAD
J042707.29-130253.6	2.1652 \pm 0.0001 ^c	731.73	343.0 \pm 1.5	47.7 \pm 3.1	32.8 \pm 3.2	39.2 \pm 1.9	29.2 \pm 2.2	SQUAD
J044017.16-433308.5	2.8582 \pm 0.0001 ^c	673.15	1210.1 \pm 2.5	86.6 \pm 5.2	48.3 \pm 5.3	397.9 \pm 3.2	382.8 \pm 3.6	SQUAD
J044821.74+095051.4	2.1093 \pm 0.0002 ^c	-350.20	1654.1 \pm 10.5	678.2 \pm 18.4	656.7 \pm 17.9	1507.4 \pm 12.9	1449.0 \pm 10.3	SQUAD
J044821.74+095051.4	2.1093 \pm 0.0002 ^c	348.42	2333.1 \pm 13.9	1463.7 \pm 24.9	1661.7 \pm 19.7	< 1779.6 \pm 14.0	1000.6 \pm 19.7	SQUAD
J053007.95-250329.7	2.813 ^h	-153.99	22508.4 \pm 6.2	821.8 \pm 0.8	625.4 \pm 0.9	184.4 \pm 1.5	94.3 \pm 1.5	SQUAD
J100731.40-333305.7	1.8362 \pm 0.0005 ^c	222.17	1120.2 \pm 33.6	824.0 \pm 21.0	760.6 \pm 21.9	917.4 \pm 37.2	883.9 \pm 43.8	SQUAD
J234628.26+124858.1 ^f	2.515	4624.79	441.2 \pm 13.2	45.2 \pm 1.7	38.2 \pm 1.8	191.3 \pm 2.2	121.9 \pm 2.6	SQUAD
J234819.19+005717.5	2.1551 \pm 0.0002 ^c	1196.90	434.4 \pm 3.4	84.2 \pm 7.2	48.0 \pm 7.4	99.0 \pm 3.0	87.9 \pm 3.9	SQUAD
J235034.25-432559.6	2.8893 \pm 0.0001 ^b	611.50	273.6 \pm 0.2	3.9 \pm 0.9	2.5 \pm 0.9	260.2 \pm 0.2	201.5 \pm 0.3	SQUAD
J092759.26+154321.3	1.8073 \pm 0.0010 ^g	-8052.61	< 14571.6 \pm 136.3	423.9 \pm 13.0	291.6 \pm 12.4	391.1 \pm 13.6	331.3 \pm 10.3	KODIAQ
J093857.01+412821.2	1.9624 \pm 0.0003 ^g	-2485.81	493.7 \pm 5.6	174.8 \pm 3.7	114.7 \pm 4.2	986.3 \pm 4.3	913.2 \pm 5.9	KODIAQ
J120147.91+120630.2	3.5219 \pm 0.0006 ^b	292.59	1352.3 \pm 1.7	376.5 \pm 4.4	278.1 \pm 3.4	223.4 \pm 3.0	134.7 \pm 3.4	KODIAQ
J145435.18+094100.0	1.9515 \pm 0.0008 ^g	174.89	< 748.1 \pm 3.4	277.6 \pm 6.5	188.9 \pm 10.6	< 651.6 \pm 5.1	< 542.5 \pm 6.1	KODIAQ
J160455.40+381201.0	2.5371 \pm 0.0007 ^g	1456.64	643.1 \pm 0.4	148.1 \pm 0.0	103.2 \pm 0.0	16.3 \pm 0.0	8.5 \pm 0.4	KODIAQ
J234628.26+124858.1 ^f	2.515	4630.81	437.7 \pm 0.0	38.7 \pm 0.0	23.6 \pm 0.0	183.6 \pm 0.0	116.8 \pm 0.0	KODIAQ

^a The mean velocity of the Si IV λ 1393 absorption trough weighted by its absorption depth.

^b The redshifts are determined using UVES spectra by the O I λ 1302.168 emission line.

^c The redshifts are determined using UVES spectra by the C III emission line.

^d The redshifts are determined using TripleSpec spectrum by the [O III] emission line.

^e The redshifts are determined using UVES spectra by the Mg II emission line.

^f This source has been observed by both UVES and KODIAQ, and the redshift, which is from the SQUAD catalog (M. T. Murphy et al. 2019), might have considerable uncertainty since the emission lines are broad and contaminated by Fe lines.

^g The redshifts are determined using SDSS spectra by the Mg II emission line.

^h The redshifts are from the SQUAD catalog (M. T. Murphy et al. 2019), which might have considerable uncertainty since the emission lines are broad.

absorber velocities are measured using the absorption profile of Si IV λ 1393.76, as listed in Table 2.

REFERENCES

- Abazajian, K. N., Adelman-McCarthy, J. K., Agüeros, M. A., et al. 2009, *ApJS*, 182, 543
- Allende Prieto, C., Lambert, D. L., & Asplund, M. 2002, *ApJ*, 573, L137
- Aoki, K., Oyabu, S., Dunn, J. P., et al. 2011, *PASJ*, 63, 457
- Arav, N., Borguet, B., Chamberlain, C., et al. 2013, *MNRAS*, 436, 3286
- Arav, N., Brotherton, M. S., Becker, R. H., et al. 2001, *ApJ*, 546, 140
- Arav, N., Liu, G., Xu, X., et al. 2018, *ApJ*, 857, 60
- Arcones, A. & Thielemann, F.-K. 2023, *A&A Rev.*, 31, 1
- Bagnulo, S., Jehin, E., Ledoux, C., et al. 2003, *Msngr*, 114, 10
- Ballero, S. K., Matteucci, F., Ciotti, L., et al. 2008, *A&A*, 478, 335
- Bell, E. F. & de Jong, R. S. 2001, *ApJ*, 550, 212
- Borguet, B. C. J., Arav, N., Edmonds, D., et al. 2013, *ApJ*, 762, 49
- Borguet, B. C. J., Edmonds, D., Arav, N., Dunn, J., & Kriss, G. A. 2012a, *ApJ*, 751, 107
- Borguet, B. C. J., Edmonds, D., Arav, N., et al. 2012b, *ApJ*, 758, 69
- Bosma, A. 1978, *PhDT*, University of Groningen
- Cameron, A. J., Fisher, D. B., McPherson, D., et al. 2021, *ApJ*, 918, L16
- Casali, M., Adamson, A., Alves de Oliveira, C., et al. 2007, *A&A*, 467, 777
- Chamberlain, C. & Arav, N. 2015, *MNRAS*, 454, 675
- Chen, H.-W., Johnson, S. D., Straka, L. A., et al. 2019, *MNRAS*, 484, 431
- Chisholm, J., Tremonti, C., & Leitherer, C. 2018, *MNRAS*, 481, 1690
- Christensen, C. R., Davé, R., Brooks, A., et al. 2018, *ApJ*, 867, 142
- Cushing, M. C., Vacca, W. D., & Rayner, J. T. 2004, *PASP*, 116, 362
- Dawson, K. S., Schlegel, D. J., Ahn, C. P., et al. 2013, *AJ*, 145, 10
- Dayal, P., Ferrara, A., & Dunlop, J. S. 2013, *MNRAS*, 430, 2891
- de Kool, M., Becker, R. H., Gregg, M. D., et al. 2002, *ApJ*, 567, 58
- Dekker, H., D’Odorico, S., Kaufer, A., et al. 2000, *Proc. SPIE*, 4008, 534
- Dimitrijević, M. S., Popović, L. Č., Kovačević, J., et al. 2007, *MNRAS*, 374, 1181
- D’Odorico, V., Cristiani, S., Romano, D., Granato, G. L., & Danese L. 2004a, *MNRAS*, 351, 976
- D’Odorico, V., Cristiani, S., Romano, D., et al. 2004b, *MSAIS*, 5, 227
- Dunn, J. P., Bautista, M., Arav, N., et al. 2010a, *ApJ*, 709, 611
- Dunn, J. P., Crenshaw, D. M., Kraemer, S. B., et al. 2010b, *ApJ*, 713, 900
- Dwek, E. 1998, *ApJ*, 501, 643
- Edmonds, D., Borguet, B., Arav, N., et al. 2011, *ApJ*, 739, 7
- Elvis, M. 2000, *ApJ*, 545, 63
- Elvis, M. 2006, *MmSAI*, 77, 573
- Elvis, M., Wilkes, B. J., McDowell, J. C., et al. 1994, *ApJS*, 95, 1
- Faber, S. M. & Gallagher, J. S. 1979, *ARA&A*, 17, 135
- Fang, T., Bryan, G. L., & Canizares, C. R. 2002, *ApJ*, 564, 604
- Ferland, G. J., Chatzikos, M., Guzmán, F., et al. 2017, *RMxAA*, 53, 385
- Ferland, G. J., Korista, K. T., Verner, D. A., et al. 1998, *PASP*, 110, 761
- Finn, C. W., Morris, S. L., Crighton, N. H. M., et al. 2014, *MNRAS*, 440, 3317
- Fitzpatrick, E. L., & Massa, D. 2007, *ApJ*, 663, 320
- Foltz, C. B., Weymann, R. J., Peterson, B. M., et al. 1986, *ApJ*, 307, 504
- Grevesse, N. & Sauval, A. J. 1998, *Space Sci. Rev.*, 85, 161
- Hall, P. B., Anderson, S. F., Strauss, M. A., et al. 2002, *ApJS*, 141, 267
- Hamann, F. 1997, *ApJS*, 109, 279
- Hamann, F. 1998, *ApJ*, 500, 798
- Hamann, F., Korista, K. T., Ferland, G. J., et al. 2002, *ApJ*, 564, 592

- Hamann, F. & Sabra, B. 2004, *ASPC*, 311, 203
- Hamann, F. W., Barlow, T. A., Chaffee, F. C., et al. 2001, *ApJ*, 550, 142
- Hambly, N. C., Collins, R. S., Cross, N. J. G., et al. 2008, *MNRAS*, 384, 637
- Hewett, P. C., Warren, S. J., Leggett, S. K., et al. 2006, *MNRAS*, 367, 454
- Hewett, P. C. & Wild, V. 2010, *MNRAS*, 405, 2302
- Hodgkin, S. T., Irwin, M. J., Hewett, P. C., et al. 2009, *MNRAS*, 394, 675
- Holweber, H. 2001, Joint SOHO/ACE workshop "Solar and Galactic Composition", 598, 23
- Hu, E. M., Kim, T.-S., Cowie, L. L., et al. 1995, *AJ*, 110, 1526
- Jiang, P., Shi, X., & Zhou, H. 2023, *Innov*, 4, 100376
- Johnstone, C. P., Güdel, M., Lüftinger, T., et al. 2015, *A&A*, 577, A27
- Kim, T.-S., Hu, E. M., Cowie, L. L., et al. 1997, *AJ*, 114, 1
- Kobayashi, C., Karakas, A. I., & Lugaro, M. 2020, *ApJ*, 900, 179
- Lai, S., Bian, F., Onken, C. A., et al. 2022, *MNRAS*, 513, 1801
- Lawrence, A., Warren, S. J., Almaini, O., et al. 2007, *MNRAS*, 379, 1599
- Liu, W.-J., Zhou, H.-Y., Jiang, N., et al. 2016, *ApJ*, 822, 64
- Lu, H., Wang, T., Yuan, W., et al. 2008, *ApJ*, 680, 858
- Lu, L., Sargent, W. L. W., Womble, D. S., et al. 1996, *ApJ*, 472, 509
- Lynds, C. R. 1967, *ApJ*, 147, 396
- Mathews, W. G. & Ferland, G. J. 1987, *ApJ*, 323, 456
- Misawa, T., Charlton, J. C., Eracleous, M., et al. 2007, *ApJS*, 171, 1
- Mo, H., van den Bosch, F. C., & White, S. 2010, *Galaxy Formation and Evolution*, by Houjun Mo, Frank van den Bosch, Simon White, 2010 (Cambridge: Cambridge Univ. Press)
- Moe, M., Arav, N., Bautista, M. A., et al. 2009, *ApJ*, 706, 525
- Murphy, M. T., Kacprzak, G. G., Savorgnan, G. A. D., et al. 2019, *MNRAS*, 482, 3458
- Netzer, H. 2015, *ARA&A*, 53, 365
- Nicastro, F., Mathur, S., Elvis, M., et al. 2005, *Nature*, 433, 495
- O'Meara, J. M., Lehner, N., Howk, J. C., et al. 2015, *AJ*, 150, 111
- O'Meara, J. M., Lehner, N., Howk, J. C., et al. 2017, *AJ*, 154, 114
- Osterbrock, D. E. & Ferland, G. J. 2006, *Astrophysics of Gaseous Nebulae and Active Galactic Nuclei*, 2nd (Sausalito, CA: Univ. Science Books)
- Pâris, I., Petitjean, P., Aubourg, É., et al. 2018, *A&A*, 613, A51
- Perrotta, S., D'Odorico, V., Prochaska, J. X., et al. 2016, *MNRAS*, 462, 3285
- Persic, M. & Salucci, P. 1995, *ApJS*, 99, 501. doi:10.1086/192195
- Peterson, B. M. 1997, *An Introduction to Active Galactic Nuclei* (Cambridge: Cambridge Univ. Press), 238
- Pettini, M. 2004, in *Cosmochemistry. The Melting Pot of the Elements*, 257, ed. C. Esteban et al. (Cambridge: Cambridge Univ. Press)
- Prochaska, J. X., Hennawi, J. F., & Herbert-Fort, S. 2008, *ApJ*, 675, 1002
- Schlegel, D. J., Finkbeiner, D. P., & Davis, M. 1998, *ApJ*, 500, 525
- Shen, Y., Brandt, W. N., Richards, G. T., et al. 2016, *ApJ*, 831, 7
- Shi, X.-H., Jiang, P., Wang, H.-Y., et al. 2016, *ApJ*, 829, 96
- Storey, P. J. & Zeippen, C. J. 2000, *MNRAS*, 312, 813
- Tian, Q., Shi, X., Hao, L., et al. 2021, *ApJ*, 914, 13
- Tian, Q., Shi, X., Lu, H., et al. 2019, *ApJ*, 877, 72
- Tumlinson, J., Peebles, M. S., & Werk, J. K. 2017, *ARA&A*, 55, 389
- Turner, M. L., Schaye, J., Steidel, C. C., et al. 2015, *MNRAS*, 450, 2067
- Vacca, W. D., Cushing, M. C., & Rayner, J. T. 2003, *PASP*, 115, 389
- Vanden Berk, D. E., Richards, G. T., Bauer, A., et al. 2001, *AJ*, 122, 549
- Veilleux, S., Cecil, G., & Bland-Hawthorn, J. 2005, *ARA&A*, 43, 769
- Veilleux, S., Meléndez, M., Tripp, T. M., et al. 2016, *ApJ*, 825, 42
- Vijayan, A., Krumholz, M. R., & Wibking, B. D. 2024, *MNRAS*, 527, 10095
- Vogt, S. S., Allen, S. L., Bigelow, B. C., et al. 1994, *Proc. SPIE*, 2198, 362
- Weymann, R. J., Morris, S. L., Foltz, C. B., et al. 1991, *ApJ*, 373, 23
- Xu, X., Arav, N., Miller, T., et al. 2018, *ApJ*, 858, 39
- Xu, X., Arav, N., Miller, T., et al. 2019, *ApJ*, 876, 105
- York, D. G., Adelman, J., Anderson, J. E., Jr., et al. 2000, *AJ*, 120, 1579
- Zafar, T., Centurión, M., Péroux, C., et al. 2014, *MNRAS*, 444, 744
- Zamorani, G., Henry, J. P., Maccacaro, T., et al. 1981, *ApJ*, 245, 357
- Zhang, S., Zhou, H., Shi, X., et al. 2015, *ApJ*, 815, 113
- Zhou, H., Shi, X., Yuan, W., et al. 2019, *Nature*, 573, 83